

A 1/8° coupled biochemical-physical Indian Ocean Regional Model: Physical results and validation

Ke Huang^{1,2} · Sergio Derada³ · Huijie Xue^{1,4} · Peng Xiu¹ · Fei Chai⁴ · Qiang Xie^{1,5} · Dongxiao Wang¹

Received: 21 October 2014 / Accepted: 20 June 2015 / Published online: 8 July 2015
© Springer-Verlag Berlin Heidelberg 2015

Abstract A coupled physical-biochemical Indian Ocean Regional Model (IORM), based on the Navy Coastal Ocean Model (NCOM) and the Carbon Silicate Nitrogen Ecosystem (CoSiNE) model was configured with the primary objective of providing an accurate estimate of the oceanic physical state along with the biochemical processes simulated by CoSiNE to understand the variability in the Indian Ocean (IO). The model did not assimilate any data; instead, weak relaxation of temperature and salinity was implemented to keep the model stable in the long-term simulations. In this study, the skill of the IORM in simulating physical states in the IO was evaluated. Basin-scale surface circulation and cross-sectional transports were compared to observations, which demonstrated that the model replicated most of the observed features with reasonably good accuracy. Consistency and biases in the upper

ocean temperature, salinity, and mixed layer depth were also analyzed. Lastly, the seasonality in the IO, its response to monsoonal forcing, and the evolution and dynamics of surface and subsurface dipole events were examined. The IORM reproduced most of the dynamic features including Ekman pumping, wave propagation, and climate variability at both annual and interannual time scales. The internal ocean dynamics and behavior of the modeled sea surface temperature anomaly (SSTA) suggest a coupled ocean/atmosphere instability that will require further research, including sensitivity experiments to realize improvements in model parameterization.

Keywords Monsoon · Seasonal and interannual variability · Indian Ocean · Arabian Sea · Surface and subsurface variability · Wave propagation

Responsible Editor: Jianping Gan

This article is part of the Topical Collection on the *6th International Workshop on Modeling the Ocean (IWMO) in Halifax, Nova Scotia, Canada 23-27 June 2014*

✉ Huijie Xue
hxue@maine.edu

- ¹ State Key Laboratory of Tropical Oceanography, South China Sea Institute of Oceanology, Chinese Academy of Sciences, Guangzhou, Guangdong, China
- ² Graduate University of Chinese Academy of Sciences, Beijing, China
- ³ Naval Research Laboratory, Stennis Space Center, Hancock, MS 39529, USA
- ⁴ School of Marine Sciences, University of Maine, 5706 Aubert Hall, Orono, ME 04469-5706, USA
- ⁵ Sanya Institute of Deep-sea Science and Engineering, Chinese Academy of Sciences, Sanya, Hainan, China

1 Introduction

The unique geographic features and monsoonal dynamics of the Indian Ocean have led to numerous studies of the region (e.g., Yamagata et al. 2004; McPhaden et al. 2009; Schott et al. 2009 and references therein). It was once believed that the Indian Ocean (IO) was a passive system simply responding to wind and thermodynamics generated in the Pacific (Yu and Rienecker 1999 and references therein). Recent research, however, has found that the IO can originate its own variability and indeed plays an active role in the natural variability of regional and global climate (Saji et al. 1999; Webster et al. 1999; Schott et al. 2009; Deser et al. 2010). Dramatic changes are associated with the Indian Ocean Dipole (IOD) events, influencing water mass distribution (Zhang et al. 2013; Du and Zhang 2015). Other prominent features of the IO include the corresponding changes of semiannual equatorial Kelvin

waves (Sprintall et al. 2000), the seasonal reversal of the Somali Current (Schott 1983; Beal et al. 2013), the anomalous coastal upwelling and ecosystem activities (Schott 1983; Wiggert et al. 2005; Liao et al. 2014), and the warmest tropical surface waters (exceeding 29 °C) (Kumar et al. 2005; Kim et al. 2012).

The northern IO consists of the Arabian Sea (AS) and the Bay of Bengal (BOB), two large bodies of water west and east of India, respectively. The AS and BOB are known as contrasting oceanographic regimes; the saline AS is dominated by evaporation and heat flux (Jensen 2003) and the fresher BOB is dominated by precipitation and river runoff (Han et al. 2001; Vinayachandran et al. 2007). Monsoon currents mix the salty and fresh waters between the AS and BOB in winter and summer (Zhang and Du 2012; Zhang et al. 2013). In the intermonsoon periods, westerlies prevail along the equator, driving a strong eastward surface jet—the Wyrтки Jet (Yoshida 1959; Wyrтки 1973; Nagura and McPhaden 2010). In the southern hemisphere, the winds are similar to those in the Atlantic and Pacific Ocean, with trade winds at low latitudes driving the South Equatorial Current (SEC) that carries the less salty water from the Indonesian straits and flows westward (Quadfasel et al. 1996; Gordon et al. 1997; Domingues et al. 2007; Sprintall et al. 2014).

The IO also experiences distinctive variability, such as the IOD (Saji et al. 1999; Webster et al. 1999; Du et al. 2013a), the Indian Ocean Basin Mode (IOBM) (Yang et al. 2007; Xie et al. 2009, 2010; Du et al. 2009, 2013b), and the monsoon-related variability in phytoplankton biomass (Hitchcock et al. 2000; Kinkade et al. 2001; Goes et al. 2005). Because of its unique features, the IO requires comprehensive and gradual analyses of its oceanographic conditions and biogeochemical processes (e.g., McCreary et al. 2009; Wiggert et al. 2009).

With the development of theories and technologies, ocean circulation models have reached a level of maturity to effectively fill the gaps in observational data. Models now allow us to explore and better understand the physical mechanisms behind various oceanic features, and in particular, for this study, we make use of the model to better understand the variability of the monsoonal circulation. However, given the wide range of spatial and temporal scales of physical and biological processes in the regional oceans, it is difficult to configure global models with sufficiently fine horizontal and vertical resolutions due to computational limitations. It is also difficult to configure all state variables to be unconstrained and free to respond to atmospheric forcing (i.e., free running), because it is challenging to keep energy/momentum balance and numerical stability during long integrations. Moreover, the inaccuracies inherent in initial and boundary conditions can cause issues of model robustness such as numerical drift. In order to overcome these difficulties, we adopted the one-way nested modeling approach of Shulman et al. (2003) in

which a global ocean general circulation model provides boundary data to a regional model that is further coupled with an ecosystem model. This approach utilizes strong relaxation at the open boundaries, but weaker relaxation in shallow waters and productive zones to allow the model to respond more freely to surface atmospheric forcing.

There have been model studies that addressed the wind-driven circulation and sea level variability in the Northern Indian Ocean and the annual cycle of the AS ecosystems with coupled physical-biochemical models (e.g., McCreary et al. 1996; Ryabchenko et al. 1998; Wiggert et al. 2006; Rahaman et al. 2014). However, to our knowledge, this is the first long-term, basin-scale simulation of the IO using a coupled physical-biochemical model. Given that the horizontal and vertical advection and diffusion play important roles in regulating the circulation of biochemical tracers, we evaluate the model skill in simulating the physical states of the ocean with an emphasis on understanding the seasonal and interannual variability of the upper ocean. The model configuration, along with datasets and comparison metrics, is described in Sect. 2; Sect. 3 presents the general features of the model simulation and the evaluation of the simulated climatological annual cycle using various observations; Sect. 4 describes the seasonality in the IO, focusing on the response to monsoonal wind and particularly the Wyrтки Jet; Sect. 5 discusses interannual variability and dipole dynamics; and Sect. 6 summarizes the results.

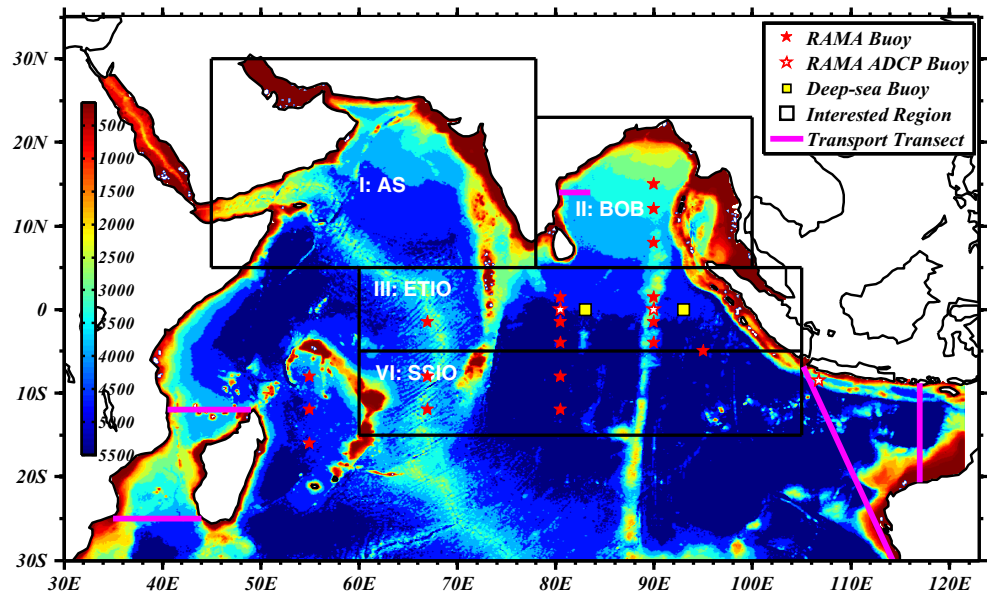
2 Model, data, and method

2.1 Model

The Indian Ocean Regional Model (IORM) is based on the Navy Coastal Ocean Model (NCOM) hydrodynamics (Martin et al. 2009) coupled to the Carbon Silicate Nitrogen Ecosystem (CoSiNE) model of Chai et al. (2002) and Dugdale et al. (2002). NCOM is similar to the Princeton Ocean Model in many ways, but it computes the free surface by an implicit scheme, and it adopts a hybrid σ - z vertical discretization, whereby terrain-following layers are used in shallow waters and z levels are used in the deep ocean. The IORM was implemented on a $1/8^\circ$ horizontal resolution Mercator grid extending from 30° S to 30° N and 30° E to 121.5° E (Fig. 1), with 40 levels in the vertical: 19 terrain-following sigma levels and 21 fixed z levels. The terrain-following levels, ranging from the surface to about 137 m, allow high vertical resolution for resolving mixed layer and shallow water dynamics. The model incorporated a realistic bathymetry and land/sea boundary (Fig. 1) derived from the NRL 2-min database.

The physical fields used for initialization and lateral boundary forcing were sea surface height (SSH), temperature, salinity, and ocean currents derived from the Global NC

Fig. 1 Model domain and bathymetry (unit: m). Several regions of interests in the IO are designated (*AS* Arabian Sea, *BOB* Bay of Bengal, *ETIO* Equatorial Tropical Indian Ocean, *SSIO* Subtropical Southern Indian Ocean), for which statistical metrics are computed throughout the study. The *pentagrams* and *yellow squares* show the moored buoy locations used for comparison, and the *thick magenta lines* show the transport transects



(Barron et al. 2006; Martin et al. 2009). Barotropic variables were constrained using the Flather radiation condition, while for the baroclinic variables, a zero-gradient condition was applied to the tangential velocity and an advective scheme was used on the normal velocity as well as the tracers. In addition, the boundary scheme was enhanced with a 10-grid cell “buffer zone” to smoothly absorb remote forcing into the domain using a half-Gaussian weighting function where the outermost boundary point had the full weight that tapers off to zero at the inner 10th grid cell.

The continuous model run consisted of two stages: (1) a spin-up stage forced with a climatological annual cycle executed for 80 years to ensure numerical robustness and achieve statistical equilibrium and (2) an interannual simulation from 1980 to 2012, forced with the surface momentum and heat fluxes derived from the Modern Era Retrospective Analysis for Research and Applications (MERRA) dataset (Rienecker et al. 2011). The interannual (daily) MERRA data were used to construct the climatological MERRA forcing (e.g., each day of each year averaged across all years to produce a daily 366-day climatology). Freshwater fluxes, including both river forcing and evaporation-precipitation (E-P), were turned off, and instead, sea surface salinity (SSS) was relaxed to monthly values derived from the Generalized Digital Environmental Model (GDEM) version 3 (Carnes 2009). The bottom boundary conditions of the IORM included quadratic bottom drag for the momentum equations and zero flux for the temperature and salinity equations.

The configuration of this IORM simulation was designed to mimic a “nature run” such that the model could respond freely to surface atmospheric forcing. However, in order to keep the integration robust and stable for multiple decades, a relaxation scheme was implemented to constrain the model to temperature and salinity monthly climatology derived from

the GDEM version 3 (Carnes 2009). While many models relax the SSS to constrain the fresh water flux, our model was not able to run multi-decadal simulations without drift by just relaxing the SSS. To mitigate this problem, 3D relaxation was introduced with relaxation timescale (T_s) and depth scale (D_s) at 6000 h and 500 m, respectively. Both time and depth relaxations were parameterized in the e-folding form as e^{-t/T_s} and $1 - e^{-z/D_s}$, where t and z are elapsed time and depth, respectively.

This model was originally configured to study oceanic biological responses in the AS for which the model parameterization was tuned. The goal was to limit the relaxation to be the weakest possible to achieve numerical stability and statistical equilibrium, yet still mimicking a nature run. The relaxation scheme was used in both climatological and interannual simulations for consistency and continuity, but its effectiveness away from the AS warrants further evaluation and justification.

2.2 Data

Various observational data were compiled to evaluate the model and complement our scientific analysis. The modeled surface currents were compared with currents from the Ocean Surface Current Analysis (OSCAR), a satellite-based estimate of 0–30 m averaged currents on a $1/3^\circ$ Mercator grid (Bonjean and Lagerloef 2002). The sea surface temperature (SST) data came from the NOAA Extended Reconstruction Sea Surface Temperature version 3b (ERSST v3b) during 1991–2011 (Smith et al. 2008) and the World Ocean Atlas 2013 (WOA13, Locarnini et al. 2013) climatology compiled for the 1985–2012 period. The subsurface temperature and salinity were evaluated using the Japan Meteorological Agency historical ocean analysis (ISHII.v6.13, Ishii and Kimoto

2009). This dataset consists of monthly mean temperature and salinity (1991–2011) from objective analyses at standard oceanographic levels in the upper 700 m on a global $1^\circ \times 1^\circ$ grid. Temperature data from several expendable bathythermograph (XBT) transects across the IO were used to validate the vertical thermal structures of the IORM. This dataset was extracted from the Tropical Ocean Global Atmosphere (TOGA) and the World Ocean Circulation Experiment (WOCE) XBT files provided by the Global Data Center for TOGA and WOCE XBT (<http://www.imosmest.aodn.org.au>).

To evaluate the modeled SSH, weekly altimeter observations (based on the combined TOPEX Poseidon (Jason-1) and ERS-1/ERS-2 (Envisat) satellite altimeter missions (Le Traon et al. 1998) from the Archiving, Validation, and Interpretation of Satellite Oceanographic (AVISO) product) were used. The satellite-derived salinity data were made available by the “Centre Aval de Traitement des Données SMOS” (CATDS) and only the 2011 observations were used. Monthly time series of temperature, salinity, and currents in the upper ocean were obtained from the Research Moored Array for African-Asian-Australian Monsoon Analysis and Prediction (RAMA, McPhaden et al. 2009) buoys and used for model-data comparisons.

2.3 Methods

2.3.1 Complex correlation coefficient

The complex correlation coefficients and angular displacements between the observed and modeled currents were adopted as part of our model validation. The complex correlation coefficient (ρ) between the mooring and IORM currents along with the angular displacement (θ) for a particular depth was estimated by using the approach of Kundu (1976) such that $\rho = \sqrt{\text{Re}^2 + \text{Im}^2}$, where

$$\text{Re} = \frac{\sum_t (u_t^o u_t^m + v_t^o v_t^m)}{\sqrt{\sum_t ((u_t^o)^2 + (v_t^o)^2) \sum_t ((u_t^m)^2 + (v_t^m)^2)}} \quad (1)$$

$$\text{Im} = \frac{\sum_t (u_t^o v_t^m - v_t^o u_t^m)}{\sqrt{\sum_t ((u_t^o)^2 + (v_t^o)^2) \sum_t ((u_t^m)^2 + (v_t^m)^2)}} \quad (2)$$

The corresponding angular displacement is given by

$$\theta = \tan^{-1} \frac{\sum_t (u_t^o v_t^m - v_t^o u_t^m)}{\sum_t (u_t^o u_t^m + v_t^o v_t^m)} \quad (3)$$

where u_t^m, v_t^m and u_t^o, v_t^o are denoted modeled and observed east-west and north-south components of velocity, respectively.

2.3.2 Singular value decomposition and empirical orthogonal function analysis

We present below a brief description of singular value decomposition (SVD) (empirical orthogonal functions (EOFs)). The anomaly field in matrix form is determined as follows:

$$X' = X - [1, \dots, 1]^T \bar{X} \quad (4)$$

where $[1, \dots, 1]^T$ is the (column) vector containing N ones and N is the number of stations. Using SVD, X' can be factored into

$$X' = U \Sigma V^T \quad (5)$$

The columns of U are eigenvectors (EOFs). The columns of V are the unit vectors pointing in the same direction (principal components). The diagonal elements of Σ are the amplitudes corresponding to each EOF. The eigenvalues are squares of Σ as

$$A(\lambda_1, \lambda_2, \dots, \lambda_N) = \Sigma^2 \quad (6)$$

The eigenvalue corresponding to the k th EOF is λ_k and its explained variance, written as a percentage, is

$$\frac{100 \lambda_k}{\sum_{k=1}^N \lambda_k} \quad (7)$$

3 Model results and validation

3.1 Currents and transport

3.1.1 Currents

Model-data comparisons were first conducted to evaluate IORM-simulated currents in the IO. Figure 2 shows the monthly climatology of surface currents from the IORM and OSCAR for four representative months. It is apparent that the model climatology can capture the seasonally reversing currents and the permanent SEC in the tropical IO similar to those described by Schott et al. (2009). During the northeast monsoon season (represented by January), the characteristic current features (e.g., the poleward-flowing West India Coastal Current (WICC)) are well represented in the IORM climatology (Fig. 2b). Other known currents, such as the Equatorial Counter Current (ECC), are clearly shown in both the observation and the model climatology. During July, the peak month of the southwest monsoon, the intrusion of the Summer Monsoon Current (SMC) into the southwestern BOB and the anti-cyclonic surface circulation in the BOB are well replicated in the model climatology (Fig. 2h). The strong

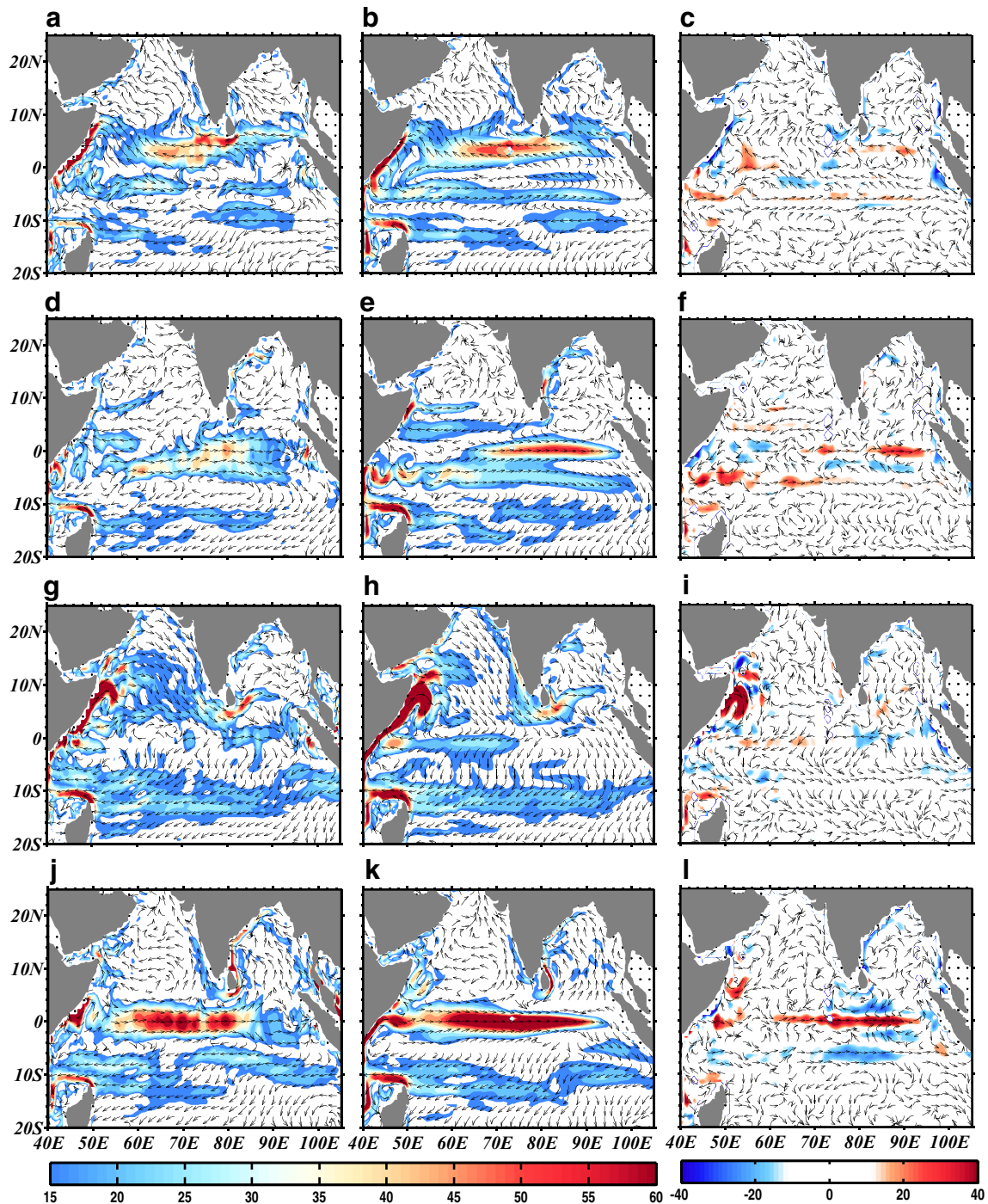


Fig. 2 Multi-year (1993–2011) averaged near surface ocean currents (unit: cm s^{-1}) derived from OSCAR observation (*left panels*) and IORM (*middle panels*) for January (**a, b**), April (**d, e**), July (**g, h**), and November (**j, k**). The right panels (**c, f, i, l**) show the biases between

IORM and OSCAR. Positive values correspond to overestimates of the IORM simulation. *Arrows* show the direction and *color shading* shows the speed of the total current

northeastward summer Somali Current can also be clearly observed in the model; however, its intensity is overestimated. The strong eastward surface jet near the equator, known as the Wyrki Jet, which develops during the monsoon transition months of April and November, is vividly seen in the model climatology with comparable magnitudes to those from

observation (Fig. 2e, k). The jet is climatically important because it carries warm and saline upper layer waters eastward, decreasing the SSH and mixed layer depth (MLD) in the west, while increasing them in the east.

Figure 2c, f, i, l shows the monthly differences between the model and observation climatology for the same months.

During the 4 months, the differences are generally less than 15 cm s^{-1} in most parts of the IO (blank area in Fig. 2c, f, i, l) and the domain-averaged differences are less than 7 cm s^{-1} . Significant differences (greater than 25 cm s^{-1}) between the model and observation are noticed near the Somalia coast in July (Fig. 2i). During the monsoon transitions, the model overestimates the strength of the equatorial currents as compared to the satellite-derived currents, and the biases show that the simulated currents are too strong in the equatorial regions (Fig. 2f, l) and too weak in the subtropical regions. This difference tends to be more pronounced in November than in other months.

Because of their relatively uninterrupted data acquisition, directly measured velocity profiles from two RAMA buoys ($0, 80.5^\circ \text{ E}$ and $0, 90^\circ \text{ E}$) were used to demonstrate the skill of the simulated subsurface currents. The zonal velocities from the observations and model, shown in Fig. 3a–d, suggest a strong semiannual cycle at the equator in the central and eastern IO. The surface flow is eastward in spring and fall through early winter (i.e., the monsoon relaxation periods), but westward in summer and late winter. Below the thermocline (between 100 and 150 m, slightly deeper at 90° E than at 80.5° E), this flow (the Equatorial Undercurrent—EUC) is reversed. Both the timing and reversal in the vertical are well represented in the model, but the magnitude of the eastward flow is slightly overestimated, as seen in Fig. 2. Figure 3e, f shows the

magnitude of complex correlation and angular displacements between the observed and modeled currents in the upper 250 m. The overall correlation is greater than 0.6, although the magnitude of the correlation between modeled and observed currents decreased with increasing depth from 150 m down, indicating a reasonable model simulation of currents. The average angle between the model predictions and observations is similar.

In summary, the model, as expected from its forcing/relaxation configuration, has good skill in simulating the upper layer currents. Despite having decreasing skill with depth, subsurface currents in the interior IO, such as the EUC, are well characterized.

3.1.2 Transect volume and heat transports

Another way to evaluate the modeled currents is to compare them with the observed mean currents in the IO. The annual mean transport through the Mozambique Channel (12° S and 25° S), the transport of the Indonesian Throughflow (ITF), and the western boundary current in the BOB obtained from the IORM are compared to previously reported values (Table 1) from a variety of sources using different reference depths and methods. For this comparison, the transport values from IORM were obtained using the reference depth that matched the corresponding studies, using a 22-year mean for

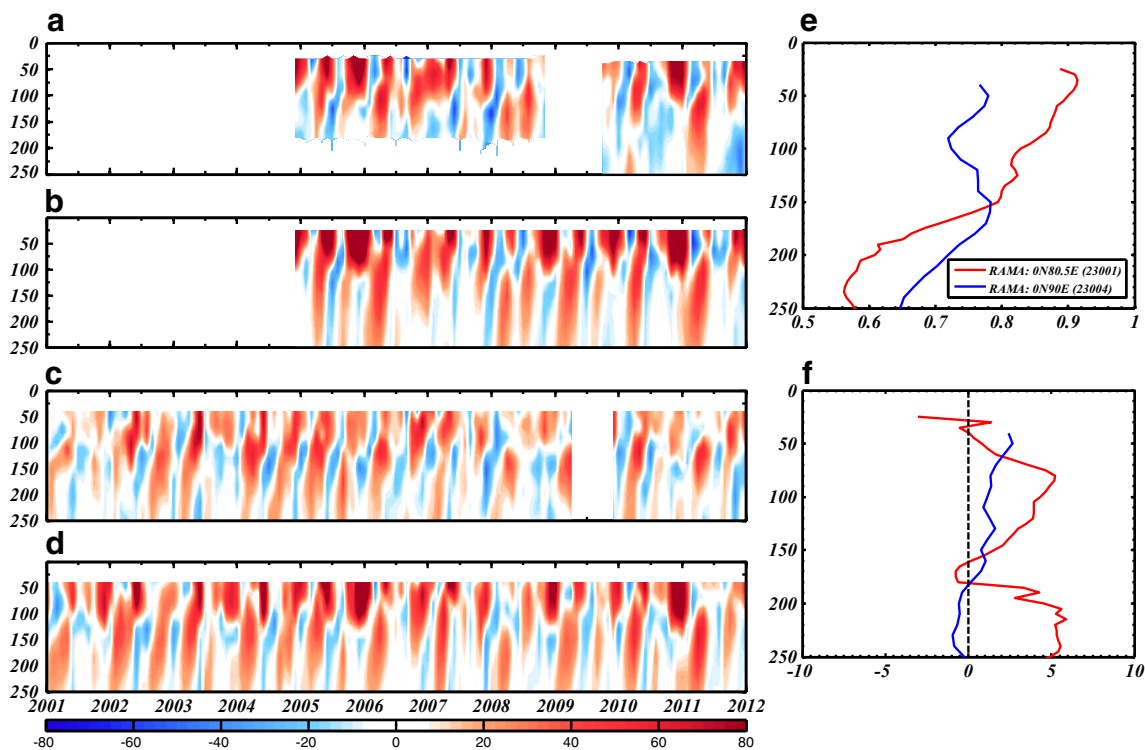


Fig. 3 Zonal velocity (unit: cm s^{-1}) at 0° N , 80.5° E derived from RAMA mooring (a) and IORM (b); zonal velocity at 0° N , 90° E derived from RAMA mooring (c) and IORM (d). Magnitude (e) and angular

displacements (f) (unit: $^\circ$) of the complex correlation between the model predicted and ADCP observed currents at these two locations

Table 1 Mean and standard deviation of IORM estimated transport (unit: Sv) through several key straits and sections in the IO in comparison with previous observations and model results

Section	Location (lat/lon/depth)	IORM		Obs/model	References
		Mean	STD		
Mozambique Channel	12° S, 40.5°–49° E (2000 m)	–25	8.0	–19.0 to –23.3	(de Ruijter et al. 2002)
	25° S, 35°–44° E (2000 m)	–24.9	6.2		
ITF	6.8° S 105.2° E–31.7° S 114.9° E (743 m)	–9.0	5.7	–9.6	(Wijffels and Meyers 2003)
Australia–Bali	8.8°–22.6° S, 117° E	–18.7	2.5	–14.6	(Barron et al. 2006)
WBC in BOB	14° N, 80°–83.5° E (March)	2.5	5.7	2	(Sanilkumar et al. 1997)

the period of 1990–2011. Overall, the modeled transports agree with the observations; some of the differences may be attributed to the interannual variability due to different observation periods and averaging intervals. The ITF (between 6.8° S, 105.2° E and 31.7° S, 114.9° E) is estimated at 9.0 ± 5.7 Sv, which is close to the annual mean of 9.6 Sv in the observations (Wijffels and Meyers 2003). The ITF and the northward flow in the subtropical gyre east of Madagascar contribute to a large transport of 25 ± 8 Sv through the Mozambique Channel. The net southward flow across 25° S is 24.9 ± 6.2 Sv, which joins the Agulhas Current. The modeled net volume transport of the Western Boundary Current in the BOB flows northward with a magnitude of 2.5 ± 5.7 Sv in March, which is consistent with previous observations in Sanilkumar et al. (1997).

The IO heat transport is important in understanding the Asian monsoon. The surface transport is generally southward on both sides of the equator during summer, but northward in winter. The net annual heat flux across the equator is southward and occurs predominantly via the cross-equatorial cell (Schott et al. 2009). Figure 4 shows the monthly meridional heat transport (in PW, $1 \text{ PW} = 10^{15} \text{ W}$) across various zonal transects from 5° S to 20° N from the simulation, which is southward from April to October, with the highest value of –2.25 PW south of the equator in June. The heat transport is northward during the rest of the year. This seasonal variability is in great agreement with previous studies (e.g., Hsiung et al. 1989; Hastenrath and Greischar 1993; Gartemicht and Schott

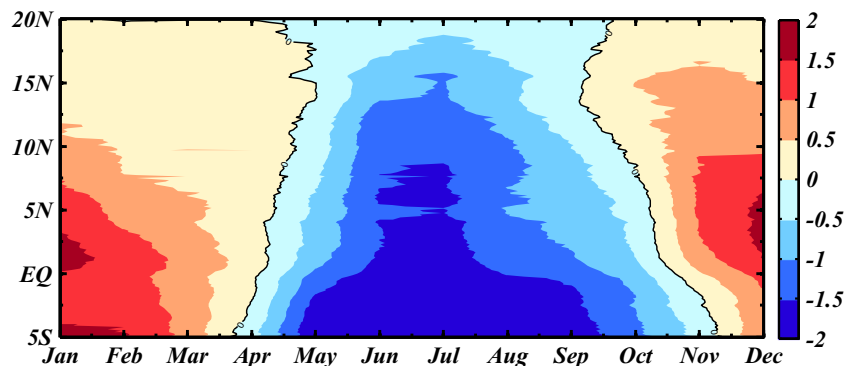
1997), but the magnitude of IORM-predicted heat transport is higher near the equatorial regions, particularly during summer (June, July, and August, 0.5 PW (33 %) higher) and winter (December, January, and February, 0.5 PW (50 %) higher) monsoon periods.

3.2 Temperature, salinity, and MLD

3.2.1 Sea surface temperature

The IO warm pool (WP) (regions with the temperature greater than 28 °C) varies greatly from season to season and it peaks in spring with the largest surface area estimated at $24 \times 10^6 \text{ km}^2$ (Kim et al. 2012). Figure 5 shows the seasonal evolution of the multi-year averaged SST patterns derived from IORM and ERSST. The model can realistically reproduce the observed seasonal cycle in the IO domain (Fig. 5a–h). In the boreal spring (MAM), a general warming is noticed and the southwestern edge of the warm pool extends towards the Madagascar region. The SST exceeds 29 °C north of the equator with the AS being the warmest place. As the upwelling along the coast of Somalia and Arabia starts to cool the western IO during the summer monsoon period, the northwestern part of the WP is progressively pushed eastward. As the southwesterly monsoon (SWM) relaxes in autumn, warming appears in the western IO, but the WP shows little change in its spatial extent. With the onset of winter cooling (December,

Fig. 4 Seasonal cycle of the meridional heat transport (unit: PW) from the IORM simulation



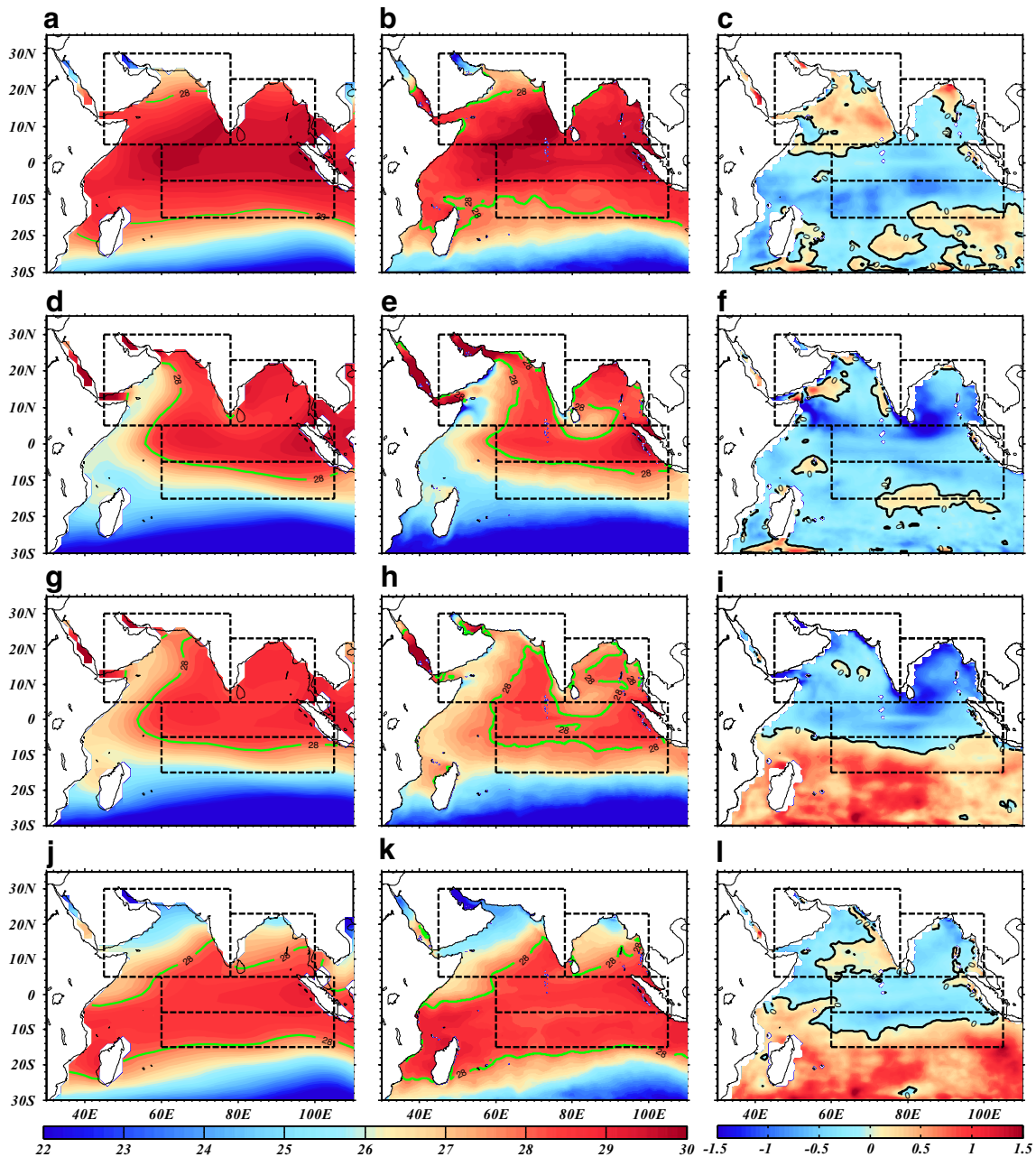


Fig. 5 ERSST (left panels) and IORM-simulated (middle panels) climatological seasonal SST (unit: °C) and their biases (right panels). Positive values in (c, f, i, l) correspond to overestimates of SST in IORM simulation.

a, b, and c represent the composite of March, April, and May; d, e, and f of June, July, and August; g, h, and i of September, October, and November; and j, k, and l of December, January, and February

January, and February), the northern extent of the WP retreats while the southwestern edge of the WP reaches the Madagascar region again. From Fig. 5a–h, it is clear that the SST evolution shows variability in accordance with the seasonal solar heating of the region, the advection of cold waters from the upwelling region in summer, and the convection-driven vertical mixing during winter, as found in Santoso et al. (2010) and Kim et al. (2012).

The biases between model and observation (Fig. 5i–l) demonstrate that the modeled SST is generally cooler. The model

shows a small cool bias (> -0.5 °C) compared to the observations in the tropics. The SST differences between the model and observations in other regions are relatively larger and show a strong seasonal dependence. For example, SST in the northern end of the BOB and the whole AS shows a warm bias during the spring. The warm biases change into cold biases in the summer and fall with a maximum of around -1.2 °C outside of the Gulf of Aden and the southwestern BOB. One of the possible causes for these biases is the feedback (among wind, entrainment, and mixing), which causes

the SST variability (Xie and Carton 2004; Foltz et al. 2010). In addition, the southern hemisphere subtropical IO in the model shows warm biases during the fall and winter, possibly exacerbated by the open boundary to the south.

The IO exhibits characteristically different patterns of SST in different areas. Regional averaged SSTs in four subdomains (AS, BOB, ETIO, SSIO; as defined in Fig. 1) show that the model can capture the two peaks of the SST annual cycle in the northern IO (Fig. 6), performing better in the AS than in the BOB. The first peak signals the direct effect of the atmospheric bridge from the Pacific and the second peak signals the memory mechanism of the IO as explained by Klein et al. (1999) and Du et al. (2009). In the AS (Fig. 6a), the two SST peaks occur during the intermonsoon periods (May and October), similar to those from ERSST and World Ocean Atlas 2013 (WOA13). However, the magnitude is overestimated from January to May when compared with ERSST and WOA13, with a maximum warm bias of 0.5 °C and underestimation for the rest of the months, especially in October through December, which reaches -0.75 °C (Fig. 6a, c). The modeled monthly mean SST in the BOB (Fig. 6b) also shows a bimodal distribution with plateaus in April and October. This is similar to the seasonal cycle from ERSST and WOA13, except that the modeled primary peak occurs in April instead of May and the secondary peak is too weak. The predicted SST shows a slightly warm bias from February to April and a notable cool bias during June to December, ranging from -0.5 to -1 °C (consistent with the cool area in Fig. 5f, g). The BOB region receives excessive fresh water from precipitation and river runoff that enables relatively

strong haline stratification in the upper layer (Sengupta et al. 2006), but Howden and Murtagudde (2001) suggested that the BOB SST is not influenced by river runoff. Since the model approximates river forcing and E-P via relaxation to sea surface salinity, it could not be determined whether the SST bias is related to the fresh water flux or not.

The modeled SST in the Equatorial Tropical Indian Ocean (ETIO) is also about 0.5 °C cooler during summer and autumn (Fig. 6c). Murtagudde and Busalacchi (1999) showed that a large part of seasonal SST variability in the northern IO is due to wind stress variability. Wind stress biases in the MERRA dataset (Kennedy et al. 2011) may be culpable for the cooler modeled SST in the northern IO. In the Subtropical Southern Indian Ocean (SSIO) (Fig. 6d), the modeled SST has a cool bias in spring and summer and a warm bias in autumn, but both the cool bias and the warm bias are small in magnitude (<0.5 °C). The SSIO is not only regulated by the solar radiation but also affected by the westward South Equatorial Current (SEC) and the influx of relatively warm and fresh Pacific water via the ITF (Bray et al. 1997; Kumar et al. 2005). Since the model was configured with prescribed eastern boundary at the Indonesian straits, this may result in biased SST distributions in the SSIO.

3.2.2 Subsurface temperature

To investigate how close the modeled thermal stratification is to the real ocean, data from several ship-of-opportunity XBT transects (IX12 and IX06) across the IO were used for model-data comparisons (Fig. 7). The XBT data are ideal for

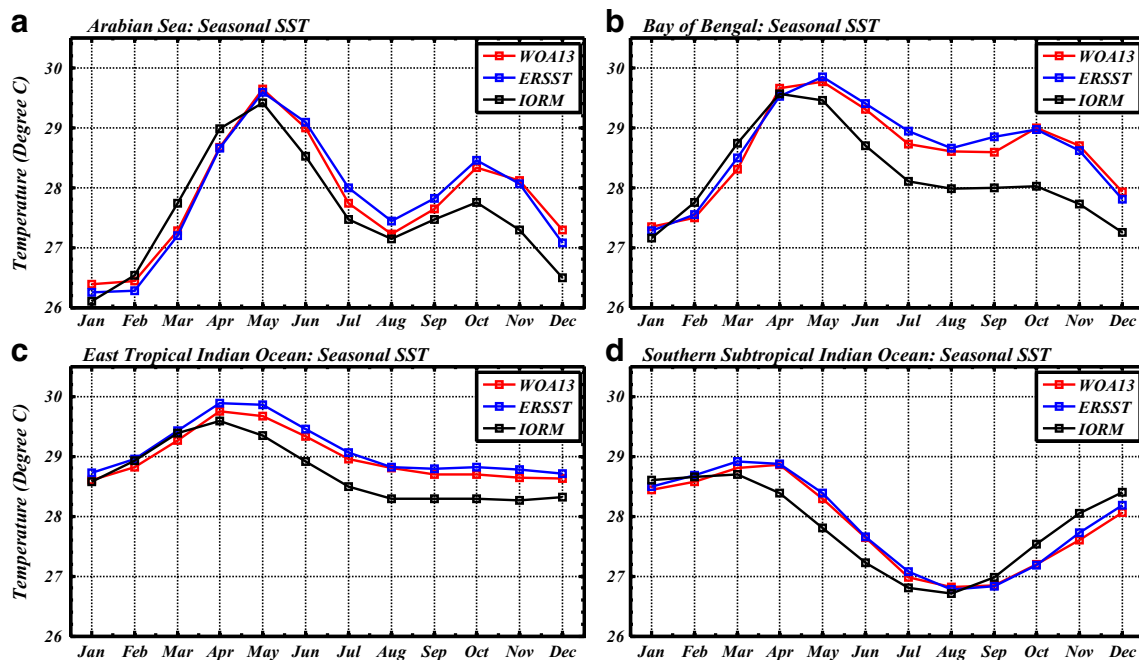


Fig. 6 Climatological seasonal cycle of SST (unit: °C) derived from WOA13 (red), ERSST (blue), and IORM (black) for four different subregions in the IO: AS (a), BOB (b), ETIO (c), and SSIO (d)

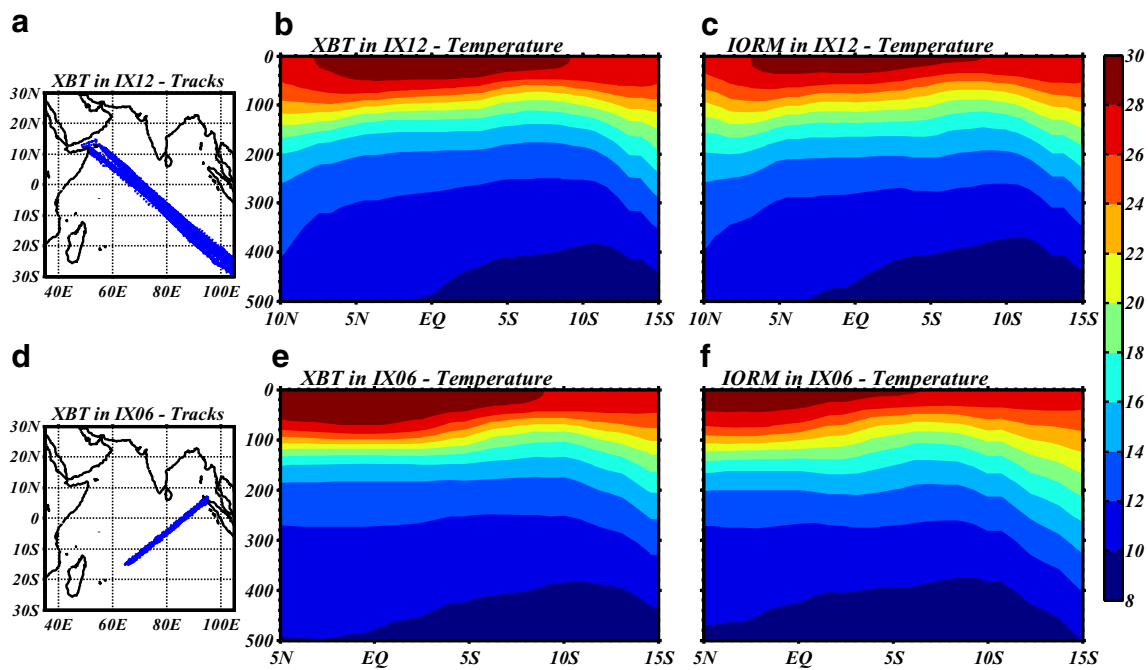


Fig. 7 XBT tracks IX12 (a) and IX06 (d) and the composite of the observed temperature (b, e) and the mean of the simulated temperature (c, f) in the upper 500 m along the tracks (unit: °C)

independent evaluations, because they were measured frequently throughout the years, and they covered very dynamic regions in the IO, with strong seasonality and interannual variability (Feng et al. 2001; Feng and Meyers, 2003). Both the climatological XBT and modeled temperature distributions show upward sloping isotherms from 15° S to 10° S and downward sloping from 10° S to 5° S associated with the SEC. The subtropical thermocline belt along 5° S plays an important role in the large-scale heat transport and climate change. The model can reproduce this subtropical thermocline belt, indicating that the IORM has the ability to simulate the response to atmospheric forcing. The differences (figures not shown), however, reveal that the modeled tropical warm water is weaker and the thermocline is more diffused. This appears to be a common problem with Oceanic General Circulation Models (OGCMs) in which diapycnal mixing is too strong because smaller vertical eddy diffusivity often leads to numerical instability (Semtner and Chervin 1988; Kumar et al. 2005).

3.2.3 Salinity

The sea surface salinity (SSS) in the IO is strongly affected by river inflow and rainfall in the BOB, the influx of low salinity Pacific water via the ITF, and the inflow of saltier water from the Red Sea. Figure 8 shows the climatology and typical year (2011) seasonal cycle of the modeled and observed SSS in the four subregions. Although the IORM has freshwater forcings (i.e., river runoff and E-P) turned off and approximated via relaxation to the SSS, and the southern boundary and the

eastern boundary at the Indonesian straits may induce rough open boundary transitions, there are no significant differences between the model and the historical climatological data. In the tropical regions, far from the open boundary and strong fresh water flux, the modeled salinity is more consistent with the observations than that in other regions. The modeled SSS has a consistent negative bias of about 0.2 psu in the AS and small biases in the BOB (from February to September), which become much larger from October to December (Fig. 8a, c). The bias in the AS is negative reaching about 0.3 psu in November and December, but it is positive in the BOB exceeding 0.5 psu in December. These biases might be due to the unrealistic treatment of fresh water in the model, particularly during the winter monsoon period. In the SSIO, the model underestimates the SSS seasonal cycle, especially during the summer from May to July (Fig. 8g), probably due to damping of signals from the ITF.

According to Ratheesh et al. (2013), more recent satellite-derived salinity products for the IO are of very good quality. The simulation appears to agree better with the satellite-derived SSS in 2011 in three out of the four subregions (not in the SSIO) (Fig. 8b, d, f, h). The seasonal cycle of the BOB in 2011 exhibits consistently higher salinity values than the climatology (Fig. 8c, d). The salinity gradients in the BOB are fresher along the coast and saltier in the center. The BOB coastal region was excluded, and only the areas with valid satellite observations were used, leading to

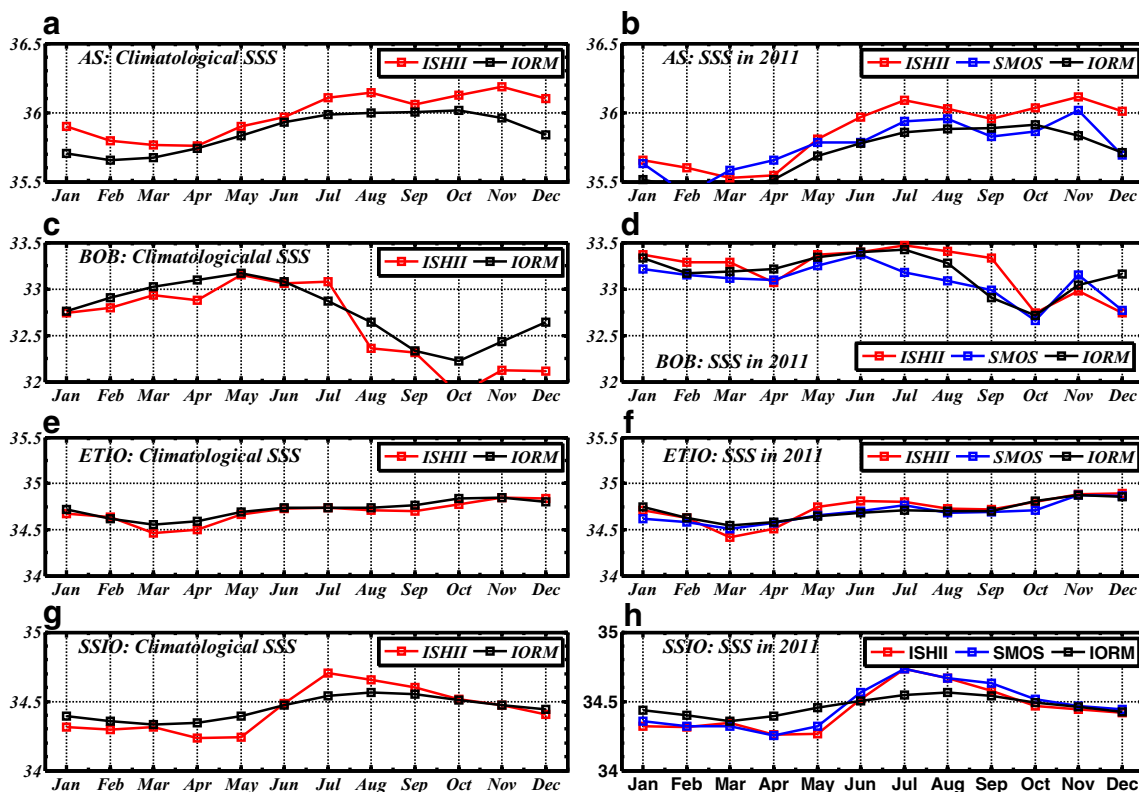


Fig. 8 Seasonal cycle of climatological SSS (Jan 1990–Dec 2011) derived from ISHII (red) and IORM (black) for four different regions (a AS, c BOB, e ETIO, g SSI). Seasonal cycle of SSS in 2011 derived

from ISHII (red), SMOS (blue), and IORM (black) for four different regions (b AS, d BOB, f ETIO, h SSI)

this unrealistic salinity differences between climatological and 2011’s SSS.

overestimated in the AS and in the BOB, especially in winter.

3.2.4 Mixed layer depth

The MLD defines the layer with quasi-homogeneous temperature, which directly interacts with the atmosphere, thermocline, and ecosystem (Foltz et al. 2010). The MLD in the IO is modulated by wind, heat, and buoyancy fluxes associated with monsoon seasonal variability. In this study, the MLD was determined using a temperature change criterion of 0.8 °C (Kara et al. 2003). The spatial patterns for the seasonal MLD were very similar between model and observation such that the MLD is deeper between 20° S and 10° S, which rises slightly from 10° S to 0°, and then deepens again (Fig. 9). In the northern IO, the MLD is deeper in summer and winter periods when monsoon winds prevail and in the interior of the AS and BOB, but shallower in coastal areas except for the northern and western AS in winter. Relative large biases (MLD is underestimated by the model) occur at the equator during summer and in the southern hemisphere subtropics during autumn. On the other hand, the MLD is

4 Wind-driven responses and seasonality in the IO

The seasonality in the upper IO circulation partly comes from wind-driven responses through local Ekman pumping and remote effects of wind-induced Rossby and Kelvin waves. Figure 10 shows the first mode of combined empirical orthogonal functions (EOFs) for monthly MERRA 10 m wind, IORM surface currents, and 20 °C isotherm depth (D20). The first combined EOF mode explains 23.9 % of the total variance of the combined data. The percentages of the total variance, explained by each variable, are 75.4 and 82.1 % for the zonal and meridional components of the MERRA wind, 32.2 and 31.2 % for the zonal and meridional components of the IORM surface currents, and 24.1 % for the IORM D20. This is primarily a seasonal mode as illustrated by the corresponding principal component (Fig. 10a).

There is a delay of approximately 3 months between the combined EOF mode and the annual cycle of the monsoon. This phase lag comes mostly from D20 because the principal components associated with the dominant mode of wind,

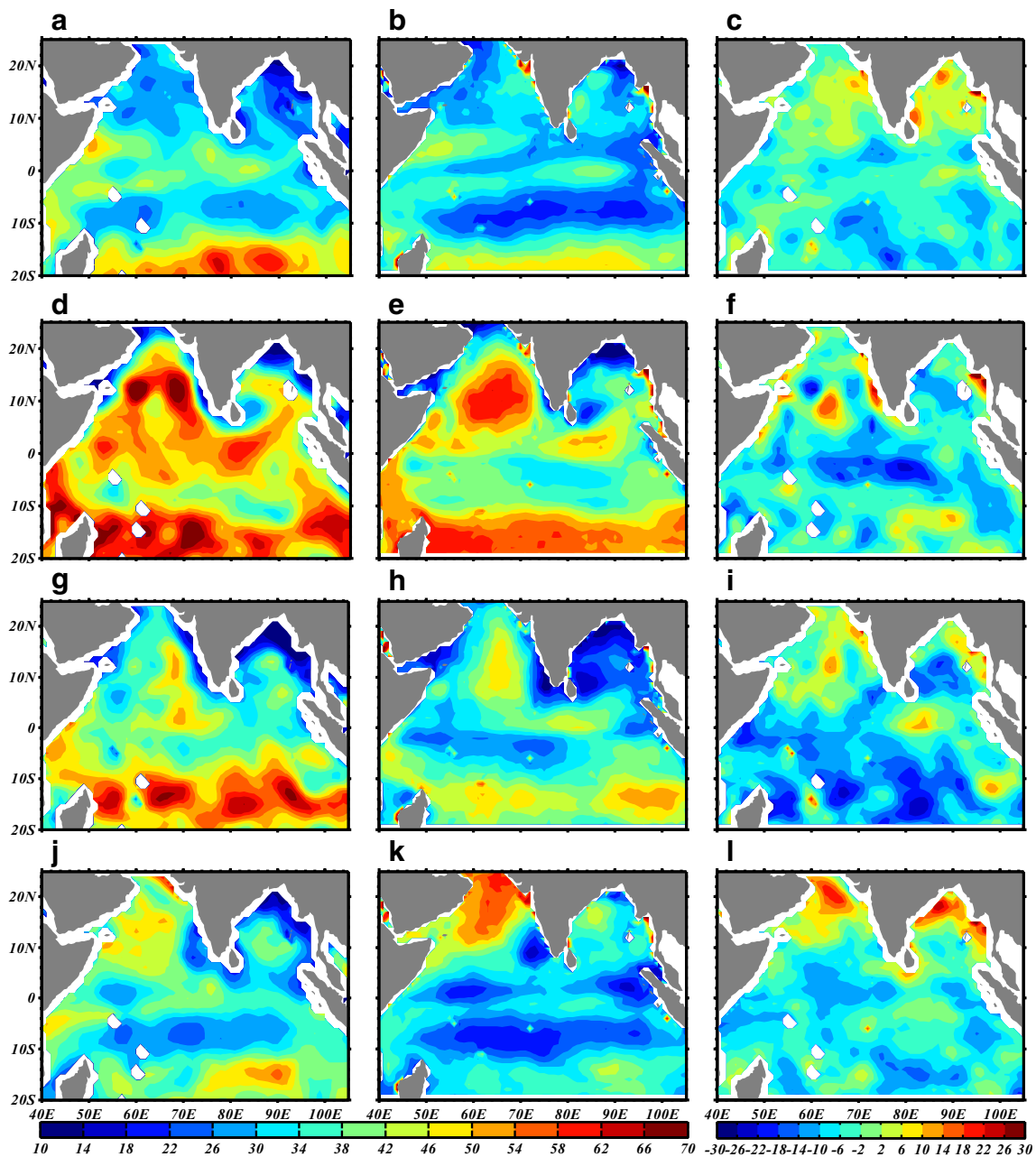


Fig. 9 Similar to Fig. 5 but for the MLD (unit: m)

surface currents, or mixed layer are in phase with the minimum in January and maximum in July (not shown). Spatially, the oscillation is characterized by the monsoon wind pattern with the winds varying markedly between the equator and 10° S (Fig. 10b). During the SWM, a dynamically important feature for the BOB is the presence of a cyclonic wind pattern in the bay and anti-cyclonic wind pattern to its south, whereas the prevailing wind in the AS is across the AS from southwest to northeast.

The corresponding patterns of the surface currents (Fig. 10c) are consistent with the wind patterns, suggesting a connection between the wind and the wind-driven currents.

Figure 10d shows the distribution of D20 that represents the subsurface ocean response to wind forcing. The connection between the D20 pattern and that of wind and currents is easy to understand. Away from equator in the interior IO, the D20 responds to the wind stress curl (Fig. 10e) such that the positive wind stress curl drives Ekman pumping thereby deepening D20 in the subtropical gyre in the southern hemisphere. The monsoon-driven Somali Current turns offshore near 10° N approximately along the zero wind stress curl line, and the cyclonic currents in the AS deepen the D20 in the interior AS. Moreover, the wind stress curl and Ekman transport drive the upwelling off

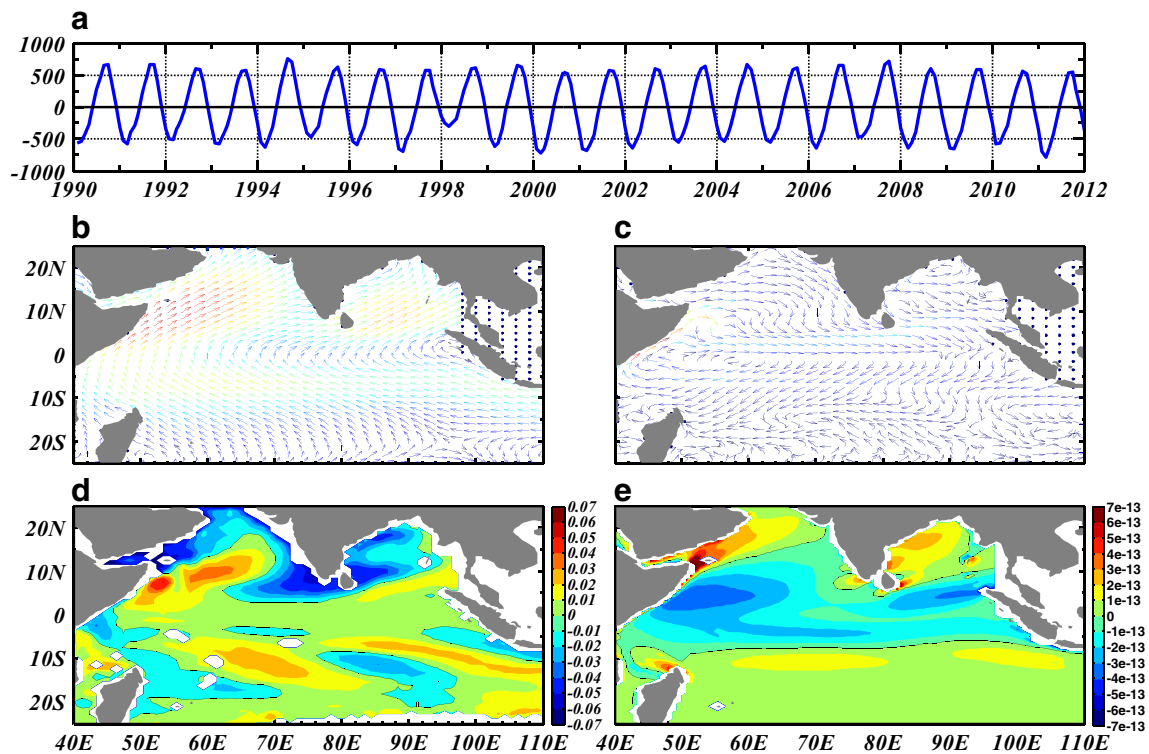


Fig. 10 **a** The principal component of the combined first EOF mode from MERRA winds, IORM currents, and thermocline depth as well as the corresponding spatial patterns for **b** MERRA winds, **c** IORM

circulation, **d** IORM thermocline depth, and **e** the curl associated with the combined first EOF mode for MERRA wind as seen in (**b**)

the Oman coast, east and west of India, and off the Sumatra-Java coast during the summer monsoon, resulting in a shallower D20 in these areas.

The aforementioned approximately 3-month phase lag in the D20 suggests a delay in subsurface response, likely related to off-equator Rossby waves, which are prominent in the southern hemisphere (Rao et al. 2002; Xie et al. 2002). To illustrate possible lateral movements of the D20 and SSH induced by wind, D20 and SSH along the 10° S transect were examined (Fig. 11). Evident both in the observation and simulation, the oceanic responses appear as the annual mutation of rising in SSH and deepening in D20, which then propagate westward as the long Rossby waves. These annual disturbances can be traced clearly to about 70° E, where it is replaced by another trains of long Rossby wave that are opposite in phase to the ones in the eastern basin but continue propagating westward at similar speeds. The signals from the two sea level and ISHII data travel at a similar speed of $\sim 0.20 \text{ m s}^{-1}$, while the signals from D20 in IORM are slightly slower at $\sim 0.16 \text{ m s}^{-1}$. The off-equatorial Rossby waves lift the sea level and deepen the D20 in the east, enhancing the west due to the propagation of downwelling. The Rossby waves generated during the annual mutation are strongly coupled to the overlying atmosphere, and the lag between the

monsoon and D20 modes (Fig. 10) is linked by off-equatorial Rossby waves.

Eastward Kelvin waves are most clearly illustrated by the D20 at the equator. Figure 12 shows time series of the MERRA zonal wind, zonal surface currents, and the D20 derived from the IORM and the RAMA buoy (0° N, 90° E). The seasonal oscillation of the thermocline and zonal current in response to zonal winds along the equatorial IO can be clearly seen. When the prevailing westerlies appear in the equatorial IO, the eastward currents are aligned with the wind patterns that are associated with a seesaw pattern for the D20 (deepening in the east and rising in the west). Conversely, easterlies cause the westward equatorial surface currents and promote the deepening in the west and rising in the east. Both the zonal surface current and the D20 from the IORM are in agreement with RAMA observations (Figs. 3c, d and 12d), with correlations of 0.76 and 0.81, respectively, indicating good skill of the IORM in capturing the annual cycle in the equatorial IO. Moreover, the Hovmöller diagram of the D20 clearly shows the eastward Kelvin waves, which take about 3 months to cross the basin, equivalent to an average phase speed of 64 cm s^{-1} , similar to that in Iskandar et al. (2006). Unlike the off-equatorial Rossby wave, the most dominant signal at the equator is the semiannual

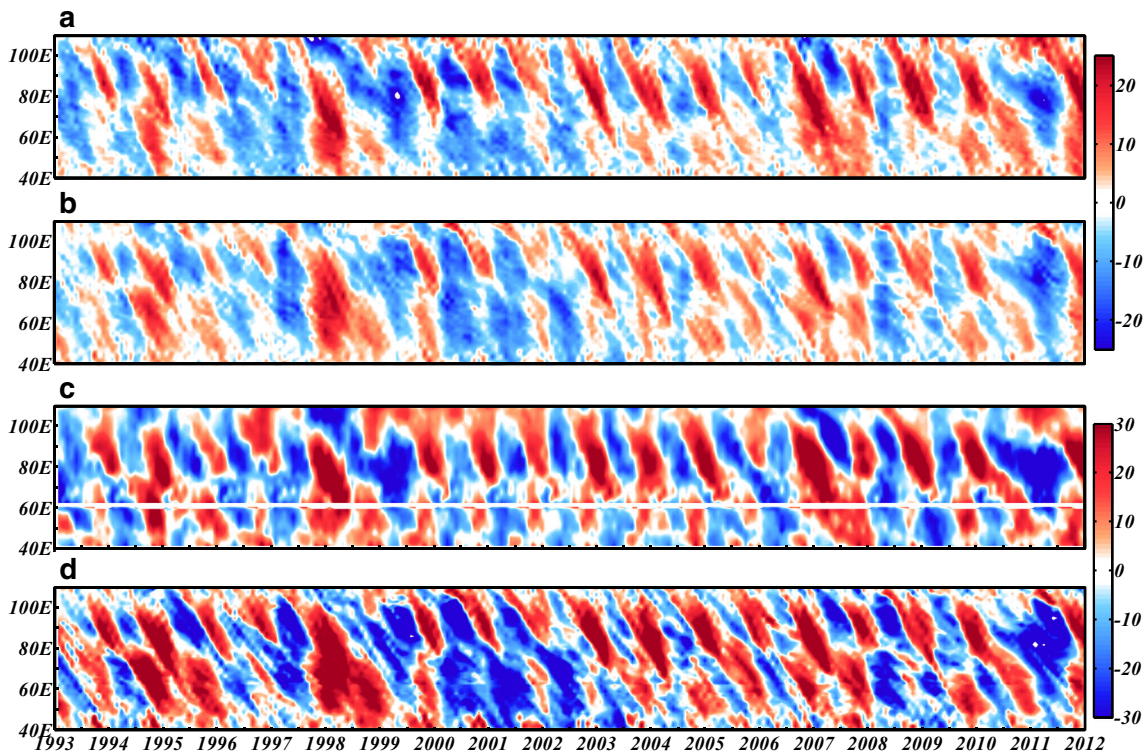


Fig. 11 Hovmöller diagram of sea level (unit: cm) derived from **a** AVISO altimeter observation and **b** IORM as well as the thermocline depth (unit: m) derived from **c** ISHII historical observation and **d** IORM along the 10° S zonal transect. The time series have been demeaned

cycle with more or less unilateral response across the basin in the zonal direction, particularly so for the

surface current. The thermocline depth, however, is biased towards the west.

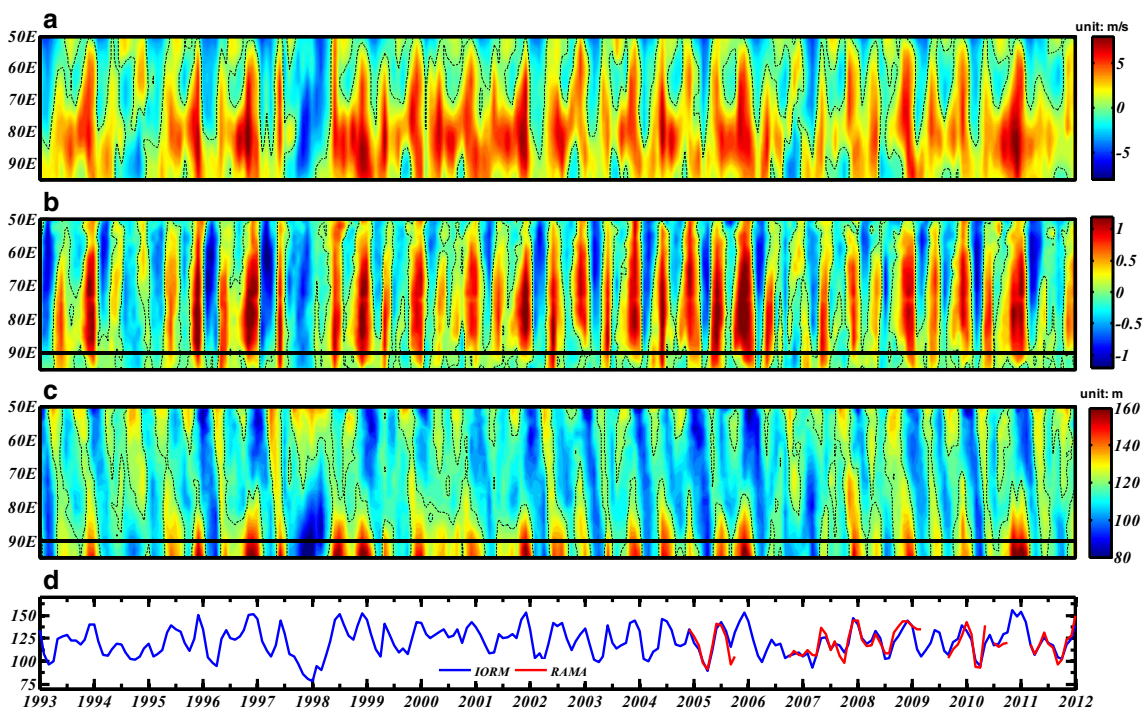


Fig. 12 Temporal evolution of monthly **a** MERRA zonal wind speed (m s^{-1}); **b** surface zonal current (m s^{-1}) obtained from IORM in the equatorial IO; **c** thermocline depth obtained from IORM in the equatorial IO; and **d** time series of thermocline depth derived from IORM (blue line) and RAMA (red line) at 0° N, 90° E

5 Interannual variability

A major part of the interannual variability in the IO is associated with the IOD, which has a much larger impact on climate variability than previously thought. For example, the IOD influences the sea surface salinity variations in the Tropical Indian Ocean (TIO) (Du and Zhang 2015), the Meridional Overturning Current in the deep IO (Wang et al. 2014), and the chlorophyll *a* concentration in the ETIO (Wiggert et al. 2009). Previous studies pointed out that the first mode of interannual variability in the SST is presented by a monopole (IOBM) and related to the ENSO, and the second dominant mode of SST is the IOD, which is locked to seasons (Saji et al. 1999; Yang et al. 2007). Unlike the SST, the first dominant mode of subsurface temperature variability is characterized by a dipole with coupled ocean/atmosphere instability (Rao et al. 2002; Feng and Meyers 2003). Its dynamics play an important role in absorbing the excess heat trapped by the greenhouse gases (Levitus et al. 2005). We noted that OGCMs are now successful in reproducing the IOD events (Iizuka et al. 2000; Lau and Nath 2004), but few of them focus on the subsurface events, which are important to the internal ocean dynamics and ecosystem variability. Hence, the simulated evolution and relationship of surface and subsurface dipole events and their dynamics are examined in this section.

5.1 Dipole mode index and surface characteristics

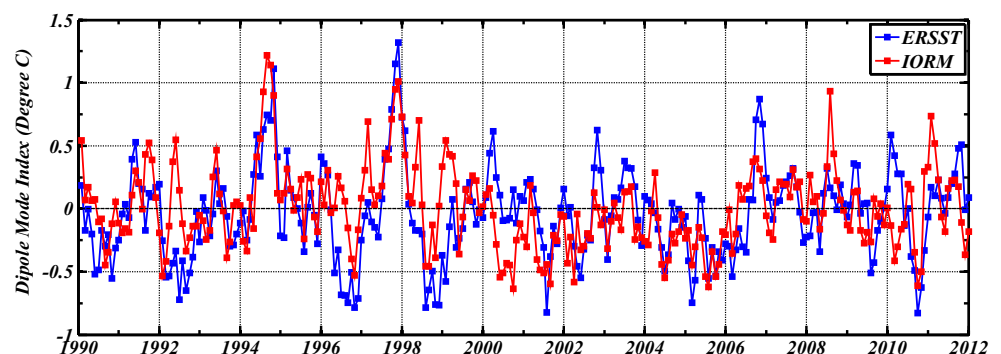
The SST dipole mode is highly influential in climate variability in the IO. According to Saji et al. (1999), the dipole mode is a striking reversal in sign of SST anomaly across the IO. The Dipole Mode Index (DMI) is defined as the SST anomaly difference between western (50° E– 70° E, 10° S– 10° N) and eastern (90° – 110° E, 10° S– 0°) Tropical Indian Ocean (Fig. 13). The results show that the IORM simulated the distinctive features of the IOD events, as in 1994, 1997, and 2006, with a variation of cold SST anomaly in the eastern IO and warm SST anomaly in the western IO during the Sumatra-Java upwelling season around June, intensifying in the following months, and peaking in October/

November. Then a warm SST anomaly in the east appears during the next upwelling season about 7 months after the eastern IO cooling. The ability of the IORM in capturing the seasonal phase locking of the IOD is evident. On the other hand, the correlation coefficient of DMIs derived from ERSST observations and IORM is 0.58, showing that the model could not meticulously simulate the evolution of dipole events, such as overestimating the 1992 cold event and the 2008 warm event. The IORM, as configured with weak SST relaxation in the upper layer, has relatively inadequate skill to capture the SST patterns in the realistic ocean, especially in the tropical eastern portion. This is also described in Ravichandran et al. (2014), showing relatively poor SST skill in the eastern IO in the absence of temperature and synthetic salinity assimilation.

The EOF analysis based on ISHII and IORM sea surface temperature anomaly (SSTA) data demonstrates further the model's ability to capture the dominant SST modes. The first EOF modes, which explain about 34.5 % of the total variance of the ISHII and 21.0 % of the IORM, are shown in Fig. 14a, d. An IOBM is clearly seen both in the observations and in the IORM, which are consistent with domain-wide response, but the maximum loading centers occur in different areas. These differences are reflected in the moderate correlation coefficient of 0.42 (Fig. 14g), suggesting that although the IORM reproduced the significant events, such as the 1997/1998 event, it had difficulty capturing all the variability of IOBM.

The second EOF exhibited a dominant east-west dipole (Fig. 14b, e) with a positive SSTA in the eastern IO and a negative SSTA in the western IO. But the spatial structures of the EOF-2 derived from ISHII and IORM show large differences, hence the poor correlation (a correlation coefficient of 0.12) for the principal components (Fig. 14h). Thus, the present model does not produce the observed surface thermal structures in the IO (see also Figs. 5 and 6). It could be due to prescribing the MERRA atmospheric heat fluxes as surface forcing to the ocean model. Analysis of the MERRA data is outside the scope of this paper, but planned sensitivity experiments will help isolate these issues further.

Fig. 13 Monthly time series of Dipole Mode Index derived from ERSST (blue line) and IORM (red line)



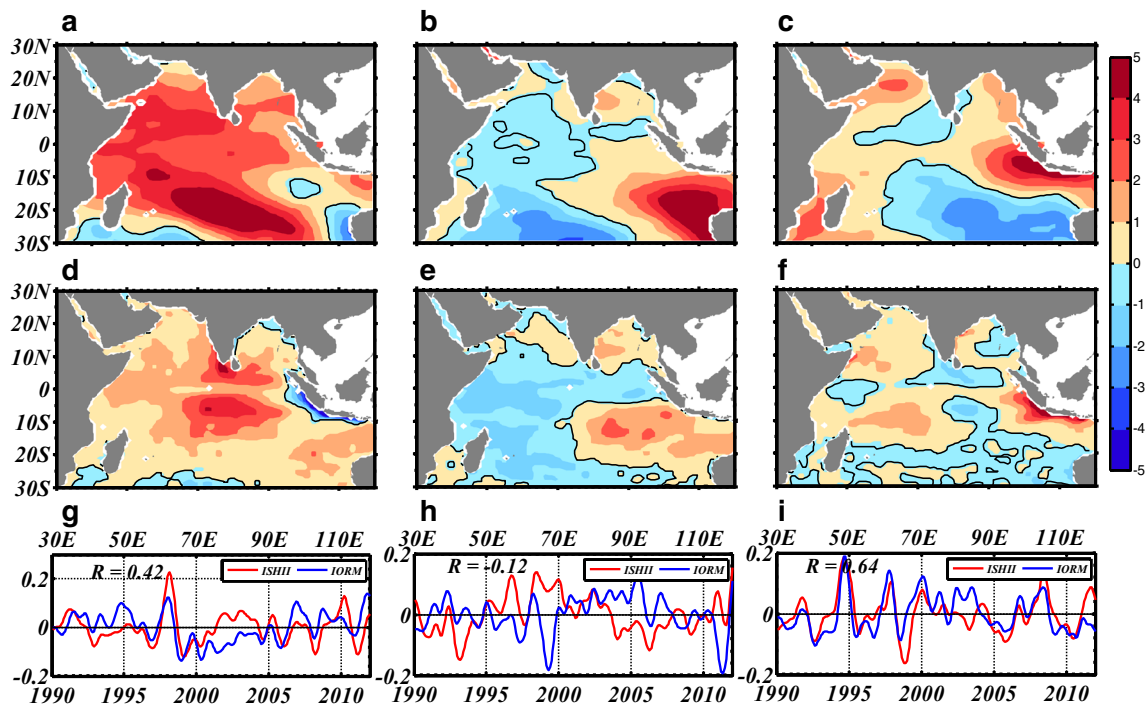


Fig. 14 The first (a, d), second (b, e), and third (c, f) EOF mode of the SSTA from ISHII (a, b, c) and IORM (d, e, f) and the principal component corresponding to the first (g), second (h) and third (i) EOF mode

5.2 Subsurface characteristics and climate connection

The evolution of the subsurface dipole resulted from coupled ocean/atmosphere instability. It is controlled by the zonal winds in the equatorial region with about a 2-month lag behind the peak phase of the IOD, providing the delayed time for reversing the phase of the surface dipole in the following year (Feng et al. 2001; Rao et al. 2002; Feng and Meyers 2003). Capturing the phase and amplitude of the subsurface dipole in the IO and its evolution is important, as it illustrates the interannual response to wind forcing, Ekman pumping, and Rossby wave propagation; all important in modulating the ecosystem variability. Figure 15 shows the interannual variability of the D20 derived from the IORM examined in conjunction with the ISHII historical observations. The results indicate that the model successfully simulates both of the two dominant modes from the observations with nearly all characteristics of each mode. The first mode of the observations with 31.18 % of the total variance is a dipole-like pattern with positive loading in the west near (10° S, 78° E) and negative loadings in the east near (5° N, 90° E and 5° S, 108° E). This is in agreement with previously observed oscillations of the D20 in the IO (Masumoto and Meyers 1998; Feng and Meyers 2003).

The second mode is the tropical saddle-shaped mode that accounts for 12.90 % of the total variance. This mode has positive loading in the southwestern tropical IO centered near (5° S, 80° E) and negative loading off the Sumatra-Java coast

and in the southeastern tropical IO centered near (15° S, 70° E and 5° S, 100° E). Although the locations and magnitude of the positive and negative centers are slightly different, the spatial patterns of the two EOF modes, derived from IORM, are very similar to the observations, with the first dipole-like pattern explaining 29.48 % of the total variance and the second saddle-shaped pattern explaining 15.25 % of the total variance. However, the modeled second mode does not capture the extension of positive loading to the southeast. The temporal correlation coefficients between observations and simulations reach 0.93 for the first mode and 0.85 for the second mode, and both pass the 99 % significance test.

Another variable of climate importance is the upper ocean heat content (HC). The Intergovernmental Panel on Climate Change (IPCC) AR5 WG1 (2013) reported that the changes in the upper HC play an important role in sea level variability due to the thermal expansion of seawater, and in global climatic change due to the heat exchange with the atmosphere. It was suggested that ocean warming accounts for 90 % of the energy accumulation from global warming between 1971 and 2010 and HC is a good indicator for these signals. Figure 16 presents the results of the EOF analysis of the monthly (1990–2011) 0–100 m HC in the IO (refer to the relatively shallow D20 of the IO). The first two EOFs for HC (calculated from the historical ISHII data) represent 44.5 and 12.1 % of the total variance, respectively. The EOF-1 shows a zonal dipole structure: positive loading in the western IO with a warm center located northeast of Madagascar and negative loading in the

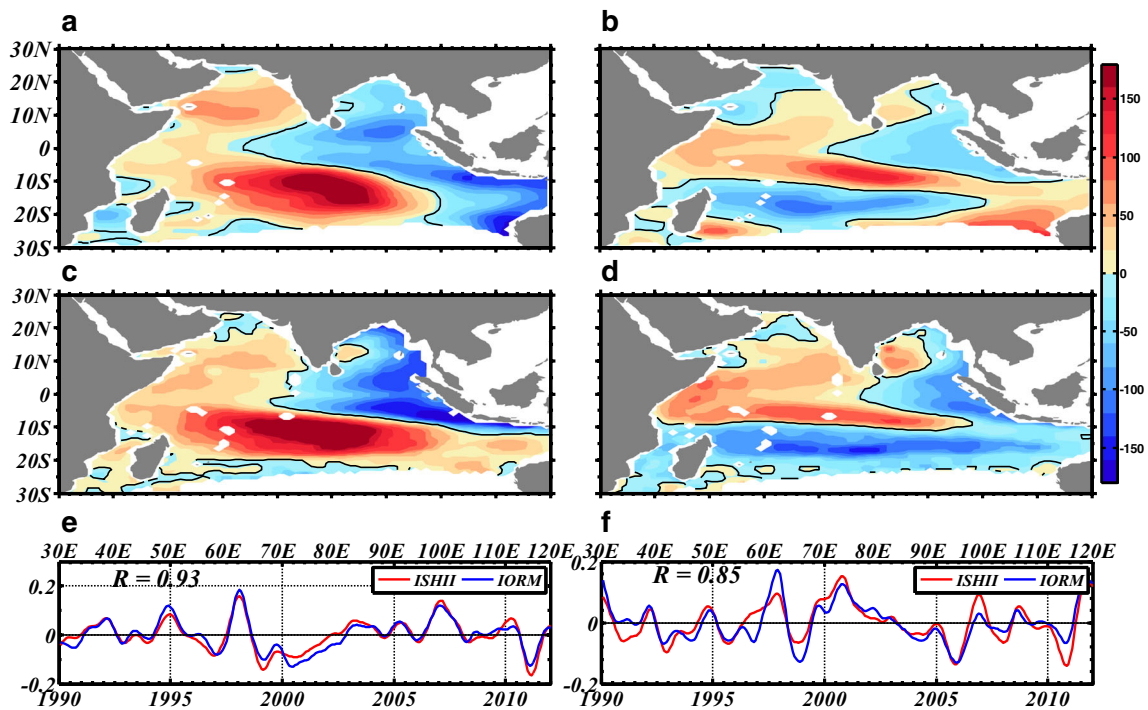


Fig. 15 The first (a, c) and second (b, d) EOF mode of the thermocline depth (20 °C isotherm: D20; unit: m) anomaly from ISHII (a, b) and IORM (c, d) and the principal component corresponding to the first (e) and second (f) EOF mode

eastern IO with a cold center located west of Sumatra-Java coast. This pattern corresponds to the positive zonal dipole event and shows similarities to the patterns obtained from the temperature at 100 m (not shown) and the D20 (Fig. 15).

The second mode shows a different zonal structure: part of the western IO is positive with a maximum located near Madagascar and a large part of the central IO is negative with a minimum value appearing near (10° S, 80° E). The IORM is

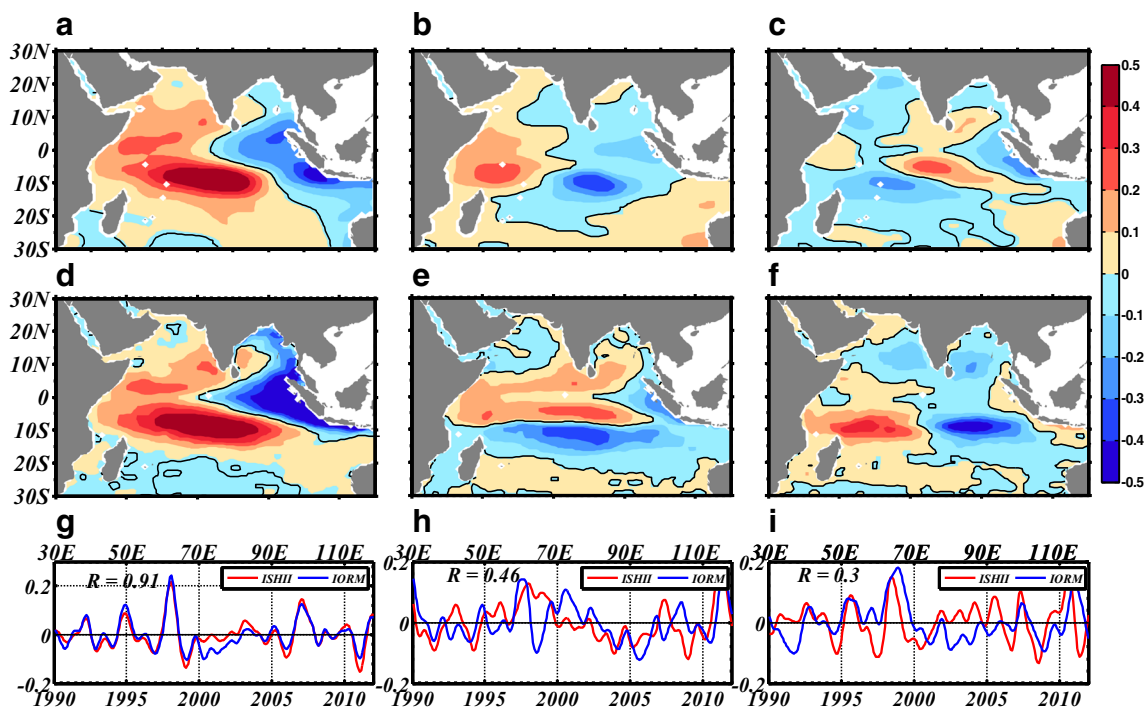
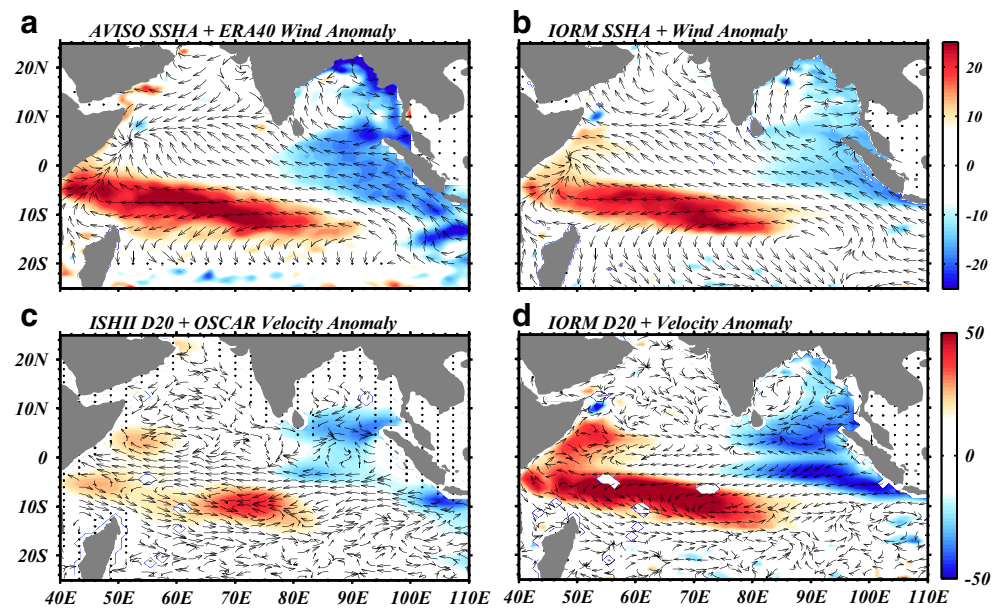


Fig. 16 The first (a, d), second (b, e), and third (c, f) EOF mode of the upper ocean (0–100 m) heat content anomaly from ISHII (a, b, c) and IORM (d, e, f) and the principal component corresponding to the first (g), second (h), and third (i) EOF mode

Fig. 17 Sea surface height anomaly (SSHA) (unit: cm, *shaded*) obtained from **a** AVISO and **b** IORM overlaid with wind anomaly (unit: m s^{-1} , *vector*) obtained from **a** ERA40 and **b** MERRA. Thermocline depth anomaly (unit: m, *shaded*) obtained from **c** ISHII and **d** IORM overlaid with surface current vector anomaly (unit: m s^{-1} , *vector*) obtained from **c** OSCAR and **d** IORM. All fields are averaged from December 1997 to February 1998



able to capture the first EOF pattern from the ISHII HC relatively well, with a similar zonal dipole structure. The correlation coefficient of the EOF-1 between the model and ISHII is 0.91. The spatial structure of the second mode, derived from the model, is a saddle-shaped structure. It is not consistent with the ISHII counterpart and the corresponding correlation coefficient is only 0.46. However, the second (third) mode

from the modeled HC is very similar to the ISHII's EOF-3 (EOF-2), with a considerable higher correlation coefficient of 0.75 (0.82) when the principal components are switched. Since the variances explained by the model-derived EOF-2 and EOF-3 are very close (11.8 % for EOF-2 versus 10.4 % for EOF-3), it is possible that the EOF-2 and EOF-3 are interchanged.

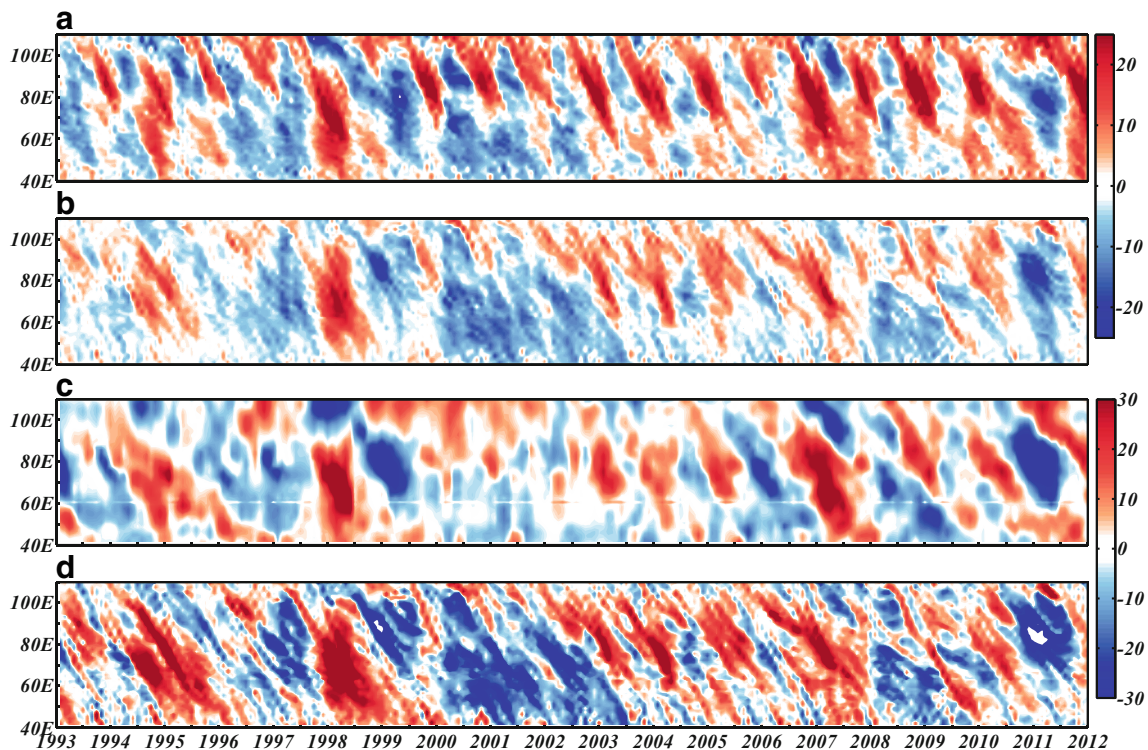


Fig. 18 Similar to Fig. 11 but for sea level anomaly (unit: cm) from **a** AVISO altimeter observation and **b** IORM as well as the thermocline depth anomaly (unit: m) from **c** ISHII historical observation and **d** IORM. The climatological annual cycle has been removed

The IORM gives good results for the fundamental characteristics of subsurface variability with the well-known dipole and saddle-shaped patterns. A connection between these patterns and the climate variability (e.g., ENSO and IOD) is further examined. The EOF-1 for the thermocline anomaly suggests a teleconnection with the ENSO signal. For example, the Southern Oscillation Index (SOI) peaked at similar magnitudes in 1991/1992, 1994, 1997/1998, 2007, and 2010, while the EOF-1 mode experienced different peak values during these time periods (Fig. 15e). Moreover, there is a transition from a positive peak (2007) to a negative peak (2008) during the 2007/2008 ENSO. During the 1994, 1997, and 2006 IOD, the first principal component lags behind the DMI by 2 to 3 months, similar to Rao et al. (2002). The temporal coefficient of the EOF-2 mode (Fig. 15f) from the IORM predicted D20 anomaly had large magnitudes related to the 1994/1995, 1997/1998, and 2011 IOD events.

5.3 Peak phase of subsurface dipole event in 1997/1998

A strong positive subsurface dipole event occurred during 1997/1998. It was characterized by deeper (shallower) than normal D20 and enhanced (suppressed) accumulation of warm water in the western (eastern) TIO. As seen in Fig. 17, the IORM is able to reproduce the peak phase of the dipole structure observed by Huang and Kinter (2002). The wind anomaly and associated Ekman pumping generate off-equatorial Rossby waves that travel westward, accumulate warm water, and deepen the thermocline in the western IO, causing the peak of a subsurface dipole event. The processes of the air-sea interactions, which explain the evolution of the subsurface dipole, are reproduced by the IORM with great spatial correspondence. However, the thermocline anomalies (deeper in the west and shallower in the east) are relatively stronger in the IORM when compared to the ISHII historical observations (Fig. 17c, d).

5.4 Role of long waves in the evolution of subsurface dipole

The evolution of the thermal structure in the IO is dominated by off-equatorial Rossby waves (Xie et al. 2002). This demonstrates the significant role of these waves in the evolution of the subsurface dipole. It is evident that the IORM struggles to capture the westward propagation of Rossby waves at the interannual timescale. The zonal transect of 10° S is shown in Fig. 18 as an example. The theoretical phase speed of the first baroclinic Rossby mode is about 0.2 m s⁻¹ for the latitudinal band of 10° S–12° S (Yamagata et al. 2004). The estimated propagation phase speed derived from the IORM is ~0.16 m s⁻¹, slightly less than the value for the theoretical phase speed. For the 1997/1998 event, the off-equatorial Rossby wave lifted the sea level and deepens the thermocline in the east during the middle of 1997. The downwelling

Rossby waves from the previous year propagated to the west during the early part of 1998, which brought a warm water anomaly to the west. Such a process stimulated the significant subsurface dipole event in 1997/1998. After that, the thermocline reversed back.

As seen from Fig. 18, the amplitude of the modeled D20 anomaly is relatively stronger than those from historical observations. The amplitude of the modeled sea surface height anomaly (SSHA) is relatively weaker than those from satellite observations, implying weaker variability of the modeled SSHA in the IO. The observed and modeled behaviors of the D20, SSH, and the role of internal subsurface dynamics suggest that there are strong interactions and instabilities among them, which the IORM has some difficulty simulating accurately.

6 Conclusions

A regional Indian Ocean coupled physical-biochemical model, which is based on NCOM and CoSiNE, was configured and used to run a long-term simulation consisting of an 80-year climatological spin-up, followed by an interannual run from 1980 to 2012. In this study, we made use of the model results to evaluate a variety of the oceanic physical states in the IO. The present analysis reveals that the model simulates most of the observed features of currents, temperature, and salinity with reasonably good accuracy.

Comparison with the OSCAR data leads to the conclusion that the model reproduces the major current systems of the IO. Comparisons with actual in situ buoy observations show that the IORM is able to capture the zonal currents and high-speed currents reasonably well. However, the model overestimates both the Somali Current during the peak summer monsoon and the equatorial currents during the monsoon transition. Nevertheless, the model-simulated mass and heat transports agree with the observations.

The model also reasonably reproduced the seasonal cycle of temperature and salinity. Differences between the model and observations are small in the tropical region, but with less satisfactory results near the southern boundary and along the Somalia coast during the peak summer monsoon. The modeled temperature distribution resembles the thermal structure derived from XBTs and buoys, although the thermocline in the undercurrent region appears to be more diffused. The model-predicted MLD is strikingly similar to that derived from historical observations, demonstrating that the model can estimate the MLD variability well.

The IORM also captured the interannual variability in the IO, which is driven primarily by the monsoon winds. Comparisons of the D20 and HC anomalies revealed that the IORM successfully simulates dominant dipole mode (EOF-1) and the tropical saddle mode (EOF-2). The prominent

subsurface dipole event of 1997/1998 and the off-equatorial wave propagation were examined and showed good agreement in both timing and location.

Validation of the off-line nested IORM provided a baseline assessment of its capabilities and offered guidance for future analyses of the coupled 13-component ecosystem. The modeled behavior of the SSTA and the role of internal ocean dynamics suggested a coupled ocean/atmosphere instability that motivates further research, including sensitivity tests and improvements in model configuration.

Acknowledgments This study was supported by the Strategic Priority Research Program of the Chinese Academy of Sciences (Grant No. XDA11010304), the China Scholarship Counsel (No. 201304910293), and the Natural Science Foundation of China (41476012). The modeling work was supported by NASA grant number NNX07AK82G, and the model simulations were performed at the Navy DoD Supercomputing Resource Center, Stennis Space Center, Mississippi. The authors thank Dr. Feng Zhou and Dr. Yan Du for their suggestions and comments. Thanks also to the NOAA/OSCAR group for providing satellite-derived current data. The RAMA data were provided by the TAO Project Office at NOAA/PMEL. The altimeter products are produced by SSALTO/DUACS and distributed by AVISO. XBT data are sourced from the Integrated Marine Observing System (IMOS); IMOS is supported by the Australian Government through the National Collaborative Research Infrastructure Strategy (NCRIS) and the Super Science Initiative (SSI). The satellite-derived salinity data were obtained from the “Centre Aval de Traitement des Données SMOS” (CATDS), operated for the “Centre National d’Etudes Spatiales” (CNES, France) by IFREMER (Brest, France)

References

- Barron CN, Kara AB, Martin PJ, Rhodes RC, Smedstad LF (2006) Formulation, implementation and examination of vertical coordinate choices in the Global Navy Coastal Ocean Model (NCOM). *Ocean Model* 11(3):347–375
- Beal LM, Hormann V, Lumpkin R, Foltz GR (2013) The response of the surface circulation of the Arabian Sea to monsoonal forcing. *J Phys Oceanogr* 43(9):2008–2022
- Bonjean F, Lagerloef GSE (2002) Diagnostic model and analysis of the surface currents in the tropical Pacific Ocean. *J Phys Oceanogr* 32: 2938–2954
- Bray NA, Wijffels SE, Chong JC, Fieux M, Hautala S, Meyers G, Morawitz WML (1997) Characteristics of the Indo-Pacific through flow in the eastern Indian Ocean. *Geophys Res Lett* 24:2569–2572
- Carnes MR (2009) Description and evaluation of GDEM-V 3.0. NRL Tech Report. NRL/MR/7330-09-9165
- Chai F, Dugdale RC, Peng T-H, Wilkerson FP, Barber RT (2002) One-dimensional ecosystem model of the equatorial Pacific upwelling system, part I: model development and silicon and nitrogen cycle. *Deep-Sea Res II* 49(13–14):2713–2745
- de Ruijter WP, Ridderinkhof H, Lutjeharms JR, Schouten MW, Veth C (2002) Observations of the flow in the Mozambique Channel. *Geophys Res Lett* 29(10):140–1
- Deser C, Alexander MA, Xie S-P, Phillips AS (2010) Sea surface temperature variability: patterns and mechanisms. *Annu Rev Mar Sci* 2: 115–143
- Domingues CM, Maltrud ME, Wijffels SE, Church JA, Tomczak M (2007) Simulated Lagrangian pathways between the Leeuwin Current System and the upper-ocean circulation of the southeast Indian Ocean. *Deep-Sea Res II* 54:797–817
- Du Y, Xie S-P, Hu K, Huang G (2009) Role of air-sea interaction in the long persistence of El Niño-induced North Indian Ocean warming. *J Clim* 22:2023–2038
- Du Y, Cai W, Wu Y (2013a) A new type of the Indian Ocean Dipole since the mid-1970s. *J Clim* 26:959–972
- Du Y, Xie S-P, Yang Y-L, Zheng X-T, Liu L, Huang G (2013b) Indian Ocean variability in the CMIP5 multi-model ensemble: the basin mode. *J Clim* 26:7240–7266
- Du Y, Zhang Y-H (2015) Satellite and Argo observed surface salinity variations in the tropical Indian Ocean and their association with the Indian Ocean Dipole mode. *J Clim* 28:695–713. doi:10.1175/JCLI-D-14-00435.1
- Dugdale RC, Barber RT, Chai F, Peng T-H, Wilkerson FP (2002) One-dimensional ecosystem model of the equatorial Pacific upwelling system. Part II: sensitivity analysis and comparison with JGOFS EqPac data. *Deep-Sea Res II* 49(13–14):2747–2768
- Feng M, Meyers G, Wijffels S (2001) Interannual upper ocean variability in the tropical Indian Ocean. *Geophys Res Lett* 28(21):4151–4154
- Feng M, Meyers G (2003) Interannual variability in the tropical Indian Ocean: a two-year time-scale of Indian Ocean Dipole. *Deep-Sea Res II* 50(12):2263–2284
- Foltz GR, Vialard J, Kumar BP, McPhaden MJ (2010) Seasonal mixed layer heat balance of the southwestern tropical Indian Ocean. *J Clim* 23:947–965
- Gartemicht U, Schott F (1997) Heat fluxes of the Indian Ocean from a global eddy-resolving model. *J Geophys Res* 102:21147–21159
- Goes JJ, Thoppil PG, Gomes HR, Fasullo JT (2005) Warming of the Eurasian landmass is making the Arabian Sea more productive. *Science* 308:545–547
- Gordon AL, Ma S, Olson DB, Hacke P, Field A, Talley LD, Wilson D, Baringer M (1997) Advection and diffusion of Indonesian throughflow water within the Indian Ocean South Equatorial Current. *Geophys Res Lett* 24(21):2573–2576
- Han W, McCreary JP, Kohler KE (2001) Influence of precipitation minus evaporation and Bay of Bengal rivers on dynamics, thermodynamics, and mixed layer physics in the upper Indian Ocean. *J Geophys Res-Oceans* 106(C4):6895–6916
- Hastenrath S, Greischar L (1993) The monsoonal heat budget of the hydrosphere-atmosphere system in the Indian Ocean sector. *J Geophys Res* 98:6869–6881
- Hitchcock GL, Key EL, Masters J (2000) The fate of upwelled waters in the Great Whirl, August 1995. *Deep-Sea Res II* 47:1605–1621
- Howden SD, Murtugudde R (2001) Effects of river inputs into the Bay of Bengal. *J Geophys Res* 106 (C9):19,825–19,843
- Hsiung J, Newell RE, Houghtby T (1989) The annual cycle of oceanic heat storage and oceanic meridional heat transport. *Q J R Meteorol Soc* 115:1–28
- Huang B-H, Kinter JL III (2002) Interannual variability in the tropical Indian Ocean. *J Geophys Res* 107(C11):3199. doi:10.1029/2001JC001278
- Iizuka S, Matsuura T, Yamagata T (2000) The Indian Ocean SST dipole simulated in a coupled general circulation model. *Geophys Res Lett* 27:3369–3372
- Ishii M, Kimoto M (2009) Reevaluation of historical ocean heat content variations with time-varying XBT and MBT depth bias corrections. *J Oceanogr* 65(3):287–299
- Iskandar I, Tozuka T, Sasaki H, Masumoto Y, Yamagata T (2006) Intraseasonal variations of surface and subsurface currents off Java as simulated in a high-resolution ocean general circulation model. *J Geophys Res* 111, C12015. doi:10.1029/2006JC003486
- Jensen TG (2003) Cross-equatorial pathways of salt and tracers from the northern Indian Ocean: modelling results. *Deep-Sea Res II* 50:2111–2128

- Kara AB, Rochford PA, Hurlburt HE (2003) Mixed layer depth variability over the global ocean. *J Geophys Res* 108 C3 3079 doi:10.1029/2000JC000736
- Kim ST, Yu J-Y, Lu M-M (2012) The distinct behaviors of Pacific and Indian Ocean warm pool properties on seasonal and interannual time scales. *J Geophys Res* 117, D05128. doi:10.1029/2011JD016557
- Kinkade CS, Marra J, Dickey TD, Weller R (2001) An annual cycle of phytoplankton biomass in the Arabian Sea, 1994–1995, as determined by moored optical sensors. *Deep-Sea Res II* 48:1285–1301
- Klein SA, Soden BJ, Lau NC (1999) Remote sea surface temperature variations during ENSO: evidence for a tropical atmospheric bridge. *J Clim* 12(4):917–932
- Kumar SP, Ishida A, Yoneyama K, Kumar MRR, Kashino Y, Mitsudera H (2005) Dynamics and thermodynamics of the Indian Ocean warm pool in a high-resolution global general circulation model. *Deep-Sea Res II* 52:2031–2047
- Kundu PK (1976) Ekman veering observed near the ocean bottom. *J Phys Oceanogr* 6:238–242
- Lau N-C, Nath MJ (2004) Coupled GCM simulation of atmosphere–ocean variability associated with zonally asymmetric SST changes in the tropical Indian Ocean. *J Clim* 17:245–265
- Le Traon PY, Nadal F, Ducet N (1998) An improved mapping method of multisatellite altimeter data. *J Atmos Ocean Technol* 15(2):522–534
- Levitus S, Antonov JI, Boyer TP (2005) Warming of the world ocean, 1955–2003. *Geophys Res Lett* 32, L02604. doi:10.1029/2004GL021592
- Liao X-M, Du Y, Zhan H-G, Shi P, Wang J (2014) Summer time phytoplankton blooms and surface cooling in the western south equatorial Indian Ocean. *J Geophys Res Oceans* 119:7687–7704. doi:10.1002/2014JC010195
- Locarnini RA, Mishonov AV, Antonov JI, Boyer TP, Garcia HE, Baranova OK, Zweng MM, Paver CR, Reagan JR, Johnson DR, Hamilton M, Seidov D (2013) World ocean atlas 2013 volume 1: temperature. In: Levitus S, Mishonov E Technical (eds) NOAA Atlas NESDIS, **73 40 pp**
- Martin PJ, Barron CN, Smedstad LF, Campbell TJ, Wallcraft AJ, Rhodes RC, Rowley C, Townsend TL, Carroll SN (2009) User's Manual for the Navy Coastal Ocean Model (NCOM) version 4.0 NRL Report NRL/MR/7320-09-9151
- Masumoto Y, Meyers G (1998) Forced Rossby waves in the southern tropical Indian Ocean. *J Geophys Res* 103(C12):27589–27602
- McCreary JP, Kohler KE, Hood RR, Olson DB (1996) A four-component model of biological activity in the Arabian Sea. *Prog Oceanogr* 37:193–240
- McCreary JP, Murtugudde R, Vialard J, Vinayachandran PN, Wiggert JD, Hood RR, Shankar D, Shetye SR (2009) Biophysical processes in the Indian Ocean. In *Indian Ocean biogeochemical processes and ecological variability*. *Geophys Monogr Ser* 185:9–32 AGU Washington DC
- McPhaden MJ, Meyers G, Ando K, Masumoto Y, Murty VSN, Ravichandran M, Syamsudin F, Yu L, Yu W-D (2009) RAMA: The Research Moored Array for African-Asian-Australian Monsoon Analysis and Prediction. *Bull Am Meteorol Soc* 90:459–480
- Murtugudde R, Busalacchi AJ (1999) Interannual variability of the dynamics and thermodynamics of the tropical Indian Ocean. *J Clim* 12:2300–2326
- Nagura M, McPhaden MJ (2010) Wyrтки Jet dynamics: seasonal variability. *J Geophys Res* 115, C07009. doi:10.1029/2009JC005922
- Quadfasel D, Frische A, Cresswell G (1996) The circulation in the source area of the South Equatorial Current in the eastern Indian Ocean. *J Geophys Res-Ocean* 101(C5):12483–12488
- Rahaman R, Ravichandran M, Sengupta D, Harrison MJ, Griffies SM (2014) Development of a regional model for the North Indian Ocean. *Ocean Model* 75:1–19
- Rao SA, Behera SK, Masumoto Y, Yamagata T (2002) Interannual subsurface variability in the tropical Indian Ocean with a special emphasis on the Indian Ocean Dipole. *Deep-Sea Res II* 49(7):1549–1572
- Ratheesh S, Mankad B, Basu S, Kumar R, Sharma R (2013) Assessment of satellite-derived sea surface salinity in the Indian Ocean. *IEEE Geosci Remote Sens Lett* 10(3):428–431
- Ravichandran M, Behringer D, Sivareddy S, Girishkumar MS, Chacko N, Harikumar R (2014) Evaluation of the global ocean data assimilation system at INCOIS: the tropical Indian Ocean. *Ocean Model* 69:123–135. doi:10.1016/j.ocemod.2013.05.003
- Rienecker MM, Suarez MJ, Gelaro R, Todling R, Bacmeister J et al. (2011) MERRA: NASA's Modern-Era Retrospective Analysis for Research and Applications. *J Clim* 24:3624–3648. doi:10.1175/JCLI-D-11-00015.1
- Ryabchenko VA, Gorchakov VA, Fasham MJR (1998) Seasonal dynamics and biological productivity in the Arabian Sea euphotic zone as simulated by a three-dimensional ecosystem model. *Glob Biogeochem Cycles* 12:501–530
- Saji NH, Goswami BN, Vinayachandran PN, Yamagata T (1999) A dipole mode in the tropical Indian Ocean. *Nature* 401:360–363
- Sanilkumar KV, Kuruvilla TV, Jogendranath D, Rao RR (1997) Observations of the Western Boundary Current of the Bay of Bengal from a hydrographic survey during March 1993. *Deep-Sea Res I* 44(1):135–145
- Santoso A, Gupta AS, England MH (2010) Genesis of Indian Ocean mixed layer temperature anomalies: a heat budget analysis. *J Clim* 15:5375–5403. doi:10.1175/2010JCLI3072.1
- Semtner AJ, Chervin RM (1988) A simulation of the global ocean circulation with resolved eddies. *J Geophys Res* 97:15502–15522
- Sengupta D, Bharath Raj GN, Shenoi SSC (2006) Surface freshwater from the Bay of Bengal runoff and Indonesian throughflow in the tropical Indian Ocean. *Geophys Res Lett* 33: L22609. doi:10.1029/2006GL027573
- Schott F (1983) Monsoon response of the Somali Current and associated upwelling. *Prog Oceanogr* 12(3):357–38
- Schott FA, Xie S-P, McCreary JP (2009) Indian Ocean circulation and climate variability. *Rev Geophys* 47(1), RG1002. doi:10.1029/2007RG000245
- Shulman IG, Kindle JC, DeRada S, Anderson SC, Penta B (2003) Development of a hierarchy of nested models to study the California current system (No. NRL/PP/7330-03-20). Naval Research Lab Stennis Space Center MS Oceanography DIV
- Smith TM, Reynolds RW, Peterson TC, Lawrimore J (2008) Improvements to NOAA's historical merged land-ocean surface temperature analysis (1880–2006). *J Clim* 21:2283–2296
- Sprintall J, Gordon AL, Murtugudde R, Susanto D (2000) A semiannual Indian Ocean forced Kelvin wave observed in the Indonesian seas in May 1997. *J Geophys Res-Oceans* 105(C7):17217–17230
- Sprintall J, Gordon AL, Koch-Larrouy L, Lee T, Potemra JT, Pujiana K, Wijffels SE (2014) The Indonesian seas and their impact on the coupled ocean-climate system. *Nat Geosci* 7:487–492
- Vinayachandran PN, Kurian J, Neema CP (2007) Indian Ocean response to anomalous conditions in 2006. *Geophys Res Lett* 34, L15602. doi:10.1029/2007GL030194
- Xie S-P, Annamalai H, Schott FA, McCreary JP (2002) Structure and mechanisms of South Indian Ocean climate variability. *J Clim* 15:864–878
- Xie S-P, Carton JA (2004) Tropical Atlantic variability: Patterns, mechanisms, and impacts. *Earth's Climate: The Ocean–atmosphere Interaction Geophys Monogr* 147:121–142
- Xie S-P, Du Y, Huang G, Zheng X-T, Tokinaga H, Hu K, Liu Q (2010) Decadal shift in El Niño influences on Indo-western Pacific and East Asian climate in the 1970s. *J Clim* 23(12):3352–3368

- Xie S-P, Hu K-M, Hafner J, Tokinaga H, Du Y, Huang G, Sampe T (2009) Indian Ocean capacitor effect on Indo western pacific climate during the summer following El Nino. *J Clim* 22:730–747
- Wang W-Q, Zhu X-H, Wang C-Z, Kohl A (2014) Deep meridional overturning circulation in the Indian Ocean and its relation to Indian Ocean Dipole. *J Clim* 27:4508–4520. doi:10.1175/JCLI-D-13-00472.1
- Webster PJ, Moore A, Loschnigg J, Leben R (1999) Coupled ocean–atmosphere dynamics in the Indian Ocean during 1997–1998. *Nature* 401:356–359
- Wiggert JD, Murtugudde RG, Christian JR (2006) Annual ecosystem variability in the tropical Indian Ocean: results of a coupled biophysical ocean general circulation model. *Deep-Sea Res II* 53: 644–676
- Wiggert JD, Hood RR, Banse K, Kindle JC (2005) Monsoon-driven biogeochemical processes in the Arabian Sea. *Prog Oceanogr* 65: 176–213
- Wiggert JD, Vialard J, Behrenfeld MJ (2009) Basin-wide modification of dynamical and biogeochemical processes by the positive phase of the Indian Ocean Dipole during the SeaWiFS era. In *Indian Ocean Biogeochemical Processes and Ecological Variability Geophys Monogr Ser 185:9–32* AGU Washington DC doi:10.1029/2008GM000776
- Wijffels SE, Meyers G (2003) Fifteen years of XBT measurements in the Indonesian Throughflow. Abstract IUGG General Assembly, Sapporo Japan
- Wyrtki K (1973) Equatorial jet in the Indian Ocean. *Science* 181:264–266
- Yamagata T, Behera SK, Luo J-J, Masson S, Jury MR, Rao SA (2004) Coupled ocean–atmosphere variability in the tropical Indian Ocean. In: Wang CZ, Xie S-P, Carton JA (eds) *Earth's Climate*. American Geophysical Union, Washington D.C., pp 189–211. doi:10.1029/147GM12
- Yang J, Liu Q, Xie S-P, Liu Z, Wu L (2007) Impact of the Indian Ocean SST basin mode on the Asian summer monsoon. *Geophys Res Lett* 34, L02708. doi:10.1029/2006GL028571
- Yoshida K (1959) A theory of the Cromwell current (the equatorial undercurrent) and of the equatorial upwelling—an interpretation in a similarity to a coastal circulation. *J Oceanogr Soc Jpn* 15:159–170
- Yu L-S, Rienecker MM (1999) Mechanisms for the Indian Ocean warming during the 1997–98 El Nino. *Geophys Res Lett* 26(6): 735–738
- Zhang Y-H, Du Y (2012) Seasonal variability of salinity budget and water exchange in the northern Indian Ocean from HYCOM assimilation. *Chin J Oceanogr Limnol* 30(6):1082–1092
- Zhang Y-H, Du Y, Zheng S-J, Yang Y-L, Cheng X-H (2013) Impact of Indian Ocean Dipole on the salinity budget in the equatorial Indian Ocean. *J Geophys Res Oceans* 118(10):4911–4923